Energy Storage Materials 63 (2023) 103024

Contents lists available at ScienceDirect

Energy Storage Materials

journal homepage: www.elsevier.com/locate/ensm

A resilient MXene/CNT nano-accordion framework for anode-free sodium-metal batteries with exceptional cyclic stability

Syam Kandula [a,1], Eunji Kim [b,c,1], Chi Won Ahn [b], Jinwoo Lee [c], Bongjun Yeom [d], Seung Woo Lee [e], Jinhan Cho [f,g], Hyung-Kyu Lim [h,*], Yonghee Lee [b,*], Jeong Gon Son [a,g,**]

[a] Soft Hybrid Materials Research Center, Korea Institute of Science and Technology, 5 Hwarang-ro 14-gil, Seongbuk-gu, Seoul 02792, Republic of Korea
[b] National Nano Fab Center (NNFC), Daejeon 34141, Republic of Korea
[c] Department of Chemical and Biomolecular Engineering, Korea Advanced Institute of Science and Technology (KAIST), 291 Daehak-Ro, Yuseong-Gu, Daejeon 34141 Republic of Korea
[d] Department of Chemical Engineering, Hanyang University, Seoul 04763, Republic of Korea
[e] George W. Woodruff School of Mechanical Engineering, Georgia Institute of Technology, Atlanta, GA 30332, USA
[f] Department of Chemical and Biological Engineering, Korea University, Seoul 02841, Republic of Korea
[g] KU-KIST Graduate School of Converging Science and Technology, Korea University, 145 Anam-ro, Seongbuk-gu, Seoul 02841, Republic of Korea
[h] Division of Chemical Engineering and Bioengineering, Kangwon National University, Chuncheon, Gangwon-do 24341 South Korea

ARTICLE INFO

Keywords:
Anode-free sodium-metal batteries
$Ti_3C_2T_x$/CNT NAFs
MXene
Anode-free battery
Energy storage
Plating/stripping

ABSTRACT

Anode-free sodium-metal batteries are considered one of the most promising alternatives for developing high-end batteries due to their high theoretical capacity, low cost, and high natural abundance. However, they have severe drawbacks in the form of inferior long-term cyclic stability. We engineered mechanically resilient MXene/CNT nano-accordion frameworks (NAFs) to host significant Na without dendrite development, even at high currents. The microcellular structures of MXene/CNT-NAFs possess numerous micro-sized pores and sodium nucleation sites. The synergetic effects of strong adhesion and charge transfer between MXene and CNT reduce overpotential during plating/stripping and facilitate uniform Na deposition. Resilient nano-accordion structures are compressed by capillary of Na nucleation during plating and expand during stripping, allowing long-term plating/stripping with little volume change. These benefits allow the MXene/CNT-NAFs/Na asymmetric cell to maintain its average CE at 99.7 % with capacities of 1.0 mAh·cm^{-2} at 1.0 mA·cm^{-2} for 900 h. Furthermore, MXene/CNT-NAFs symmetric cell exhibits a very low overpotential of 12.0 mV after 1,500 h with a capacity of 3.0 mAh·cm^{-2} at 3.0 mA·cm^{-2} and stores high capacities of 20.0 mAh·cm^{-2} at 5.0 mA·cm^{-2} for 1,200 h. The anode-free MXene/CNT-NAFs//$Na_3V_2(PO_4)_3$@C full-cell demonstrates exceptional long-term cyclic stability over 5,000 cycles at 5.0 C and 10.0 C without cell failure.

1. Introduction

Energy storage systems need to meet stringent design requirements, including high energy and power densities, operational safety, cyclical stability, and cost-effectiveness, to be useful in real-world applications such as automotive electrification, grid-scale technologies, defense, and aerospace engineering [1–4]. Beyond the lithium-ion battery system, metal batteries (MBs) such as lithium-metal batteries [5,6], zinc-metal batteries, and sodium-metal batteries (SMBs) [7] are continuously being developed to meet these criteria. SMBs are particularly appealing due to the abundance of sodium (2.75 % of the earth's crust) and the affordability of precursor salts (e.g., Na_2CO_3 costs approximately $0.5 kg^{-1} compared to Li_2CO_3 at around $6.5 kg^{-1}) [8,9]. Metallic Na's huge theoretical capacity of 1,166 mAh g^{-1} and its low redox potential of -2.71 V *vs.* SHE make it an intriguing candidate for future practical uses [10,11]. The metallic Na has been used as an anode in several battery types, including Na-air [12], Na-CO_2 [13], Na-sea water [14], and Na-S batteries [15]. Despite their widespread use, sodium-metal anodes have

* Corresponding authors.
** Corresponding author at: Soft Hybrid Materials Research Center, Korea Institute of Science and Technology, 5 Hwarang-ro 14-gil, Seongbuk-gu, Seoul 02792, Republic of Korea.
E-mail addresses: hklim@kangwon.ac.kr (H.-K. Lim), yhlee@nnfc.re.kr (Y. Lee), jgson@kist.re.kr (J.G. Son).
[1] S.K. and E.K. contributed equally to this work.

https://doi.org/10.1016/j.ensm.2023.103024
Received 4 September 2023; Received in revised form 10 October 2023; Accepted 19 October 2023
Available online 20 October 2023

disadvantages, including Na's high chemical reactivity and uneven charge distribution at the electrode-electrolyte interface. Thus, there is a growth of mossy-type dendrites and the creation of electrically inactive "dead Na" during repeated plating and stripping cycles, which damages the separator and ultimately leads to cell failure [10,16]. In addition, the high theoretical energy density of MBs is, in fact, not greatly benefited by a too-thick anode containing an excessive amount of active metal [17]. All of these characteristics contribute to low Coulombic efficiency (CE) during long-term cycling, resulting in a rapid loss of capacity and thus cell death.

To overcome these limitations and enhance the energy density of SMBs, the concept of anode-free SMBs (AFSMBs) has been proposed and developed [10,17–19]. In the initial cycle of AFSMBs, the anode host undergoes electrochemical plating and stripping forming a solid electrolyte interphase (SEI) on its structure, which protects it from air. Additionally, there is no loss of energy density or Na waste, as Na^+ is solely transported between the cathode and anode host. However, these AFSMBs with a limited amount of Na have critical long-term cycling issues due to Na consumption through the creation of new SEIs and the growth of dead Na, ultimately leading to cell death [20]. Several solutions have been implemented to overcome these problems. Among them, controlling the location of the initial Na nucleation site [11,21], optimizing the anion solvation structure [22], combining electrolyte additives with electrolyte solvents [23,24], and optimizing the SEI and cathode electrolyte interphase (CEI) with dual Na salts [17] are more appealing. However, research has not stopped at these approaches; other methods, such as the use of concentrated electrolytes [25,26], ionic liquids [27], and solid-state electrolytes [28], the tuning of nanostructured hosts [29], and the formation of artificial SEI layers on a metal anode [30–34], have also been investigated. Despite these efforts, research on AFSMBs is still in its infancy, and there have been no significant advancements that would enable its usage in real-time applications.

Two-dimensional (2D) MXene materials have aroused the interest of scientists in numerous disciplines [35–39] $Ti_3C_2T_x$ MXene has the potential to be employed as an anode host for the deposition of metals in energy storage devices on account of its high metallic electrical conductivity ($\sim 10^4$ S cm^{-1}) and ion-friendly hydrophilic property provided by the surface functional groups (OH, O, and F) [15,29,38,40–44]. Nonetheless, 2D $Ti_3C_2T_x$ film is mostly restacked during structure formation and thus has a compact, dense structure with inaccessible sites and inhomogeneous nucleation sites on the surface, which provide hotspots for the development of mossy dendrites during plating and stripping in cycling and, eventually, cell death [15,29,40]. It is inevitable to tailor the interspace of a nanostructured anode host and exert control over the initial nucleation site to maximize the performance of AFSMBs with excellent sodiophilicity and electrophilicity.

In this regard, we design resilient $Ti_3C_2T_x$/single wall carbon nanotubes (CNT) nano-accordion frameworks (NAFs) as efficient anode hosts for AFSMBs, with benefits such as: (i) $Ti_3C_2T_x$/CNT NAFs with microcellular structures create more micro-sized porous space with numerous Na nucleation sites in the anode host, permitting fast and uniform plating and stripping during cycling and maintaining a high CE; (ii) the perfect exposure of sodiophilic surface functional groups on the MXene nanoplates and CNTs can synergistically guide the deposition of Na, effectively reducing the overpotential of Na nucleation in the initial stage; (iii) by the high mechanical deformability of the nano-accordion structure resulting from the strong adhesion between MXene and CNT surfaces, the $Ti_3C_2T_x$/CNT NAFs can maintain their structural integrity with little total volume changes even under repetitive charging/discharging. All of these characteristics allow the $Ti_3C_2T_x$/CNT NAFs/Na asymmetric cell to keep their average CE at 99.7 % with a capacity of 1.0 mAh cm^{-2} at 1.0 mA cm^{-2} for 900 h. Extremely minimal overpotential, around 12.0 mV after 1,500 h with a capacity of 3.0 mAh cm^{-2} at 3.0 mA cm^{-2}, is observed in symmetric cells fabricated with $Ti_3C_2T_x$/CNT NAFs. In addition, these symmetric cells are capable of hosting a high capacity of 20.0 mAh cm^{-2} at 5.0 mA cm^{-2} for 1,200 h. Furthermore, the manufactured anode-free $Ti_3C_2T_x$/CNT NAFs//$Na_3V_2(PO_4)_3$@C full cell displays long-term cyclic stability even at a high C-rate of 5.0 C and 10.0 C without cell failure. To the best of our knowledge, this is the first instance in which anode-free $Ti_3C_2T_x$/CNT NAFs//$Na_3V_2(PO_4)_3$@C full cell exhibits such long-term cyclic stability at a high C-rate without cell failure. We hope that our research will pave the way for effective nanostructured designs to enhance the performance of AFSMBs in the future.

2. Results and discussion

The synthesis of resilient $Ti_3C_2T_x$/CNT NAFs is depicted in Scheme 1. To obtain a homogeneous mixture, aqueous dispersions of $Ti_3C_2T_x$ and CNTs were blended in a specified ratio and probe-sonicated for 10 min. The solution was then poured into a silicone rubber mold (3.0 mm thick and 16.0 mm in diameter) on a silicon wafer, afterward, which was placed on a pre-cooled copper (Cu) substrate underneath liquid nitrogen. During the directional freezing process, ice crystals as templates can develop in vertical directions after being exposed to a temperature gradient to form a porous, well-ordered 2D micro-cellular structure. After the directional freezing, freeze-drying allowed the formation of resilient $Ti_3C_2T_x$/CNT NAF structures. By pressing $Ti_3C_2T_x$/CNT NAFs on a Cu foil at a pressure of ~10,000 Psi using a carver hydraulic press, we were able to dramatically reduce the thickness of the $Ti_3C_2T_x$/CNT NAFs from 3 mm to 30 μm (Fig. S1a–c and h), thereby forming a very thin and accordion-like anode host. For the control samples, the $Ti_3C_2T_x$-only NAFs and CNT-only free-standing electrodes (FSEs) were also prepared and shown in Fig. S1d–f. The $Ti_3C_2T_x$ NAF was mechanically highly fragile and shattered into numerous pieces (Fig. S1d, e), making it difficult to conduct electrochemical studies reliably. Consequently, we utilized mechanically stable $Ti_3C_2T_x$ films for our electrochemical investigations. In contrast, CNT-only FSEs revealed that they were fluffy and had rough surfaces (Fig. S1f). The thickness of uncoated Cu and Al foils was determined to be ~20 μm. (Fig. S1g & i).

Beginning with X-ray diffraction (XRD) analysis, the structural analysis of the produced pure $Ti_3C_2T_x$, $Ti_3C_2T_x$ films, and $Ti_3C_2T_x$/CNT NAF samples was executed. The XRD patterns of pure $Ti_3C_2T_x$ and $Ti_3C_2T_x$ film are presented in the inset of Fig. S2a; it reveals four peaks at 2θ values of 7.2, 14.4, 21.6, and 28.8°, which correspond to (002), (004), (006), and (008) planes of $Ti_3C_2T_x$ [45]. The interlayer gap of pure $Ti_3C_2T_x$ and $Ti_3C_2T_x$ film is found to be approximately 12.5 and 12.0 Å when water molecules are intercalated between the layers. In comparison to pure $Ti_3C_2T_x$ and $Ti_3C_2T_x$ film, the XRD pattern of $Ti_3C_2T_x$/CNT NAFs displays a substantially weaker intensity peak at a 2θ value of 6.8° without any high order peaks and the anticipated interlayer spacing is around 13.0 Å (Fig. S2a). Successful incorporation of CNTs between the interlayers of $Ti_3C_2T_x$ limits the stacking of $Ti_3C_2T_x$ layers, which can facilitate Na deposition and electrolyte penetration in the $Ti_3C_2T_x$/CNT NAFs, as indicated by the increased interlayer separation, reduced (002) peak intensity and disappeared high order peaks. The existence of CNTs is characterized by the appearance of a broad peak between 12.0 and 30.0° in the $Ti_3C_2T_x$/CNT NAFs. To find out surface active groups in the $Ti_3C_2T_x$/CNT NAFs, we have carried out the FT-IR analysis, and the corresponding spectrum is shown in Fig. S2b. The FT-IR analysis further confirms the presence of -OH and C-F active groups on the surface of $Ti_3C_2T_x$/CNT NAFs.

Field-emission scanning electron microscopy (FESEM) was utilized to examine the morphology of pure $Ti_3C_2T_x$, $Ti_3C_2T_x$ NAFs, $Ti_3C_2T_x$ films, CNT FSEs, and $Ti_3C_2T_x$/CNT NAFs. The pure $Ti_3C_2T_x$ shows aggregated sheet-like structure with many wrinkles (Fig. S2c). The $Ti_3C_2T_x$ NAFs shows randomly distributed $Ti_3C_2T_x$ sheets but mechanically unstable porous structure (Fig. S2d). Pure $Ti_3C_2T_x$ films exhibit a sheet-like shape with folds and wrinkles (Fig. S2e). The CNT FSEs resemble a net-like porous structure (Fig. S2f). Fig. 1a and b show top-view and cross-sectional images of as-prepared $Ti_3C_2T_x$/CNT NAFs,

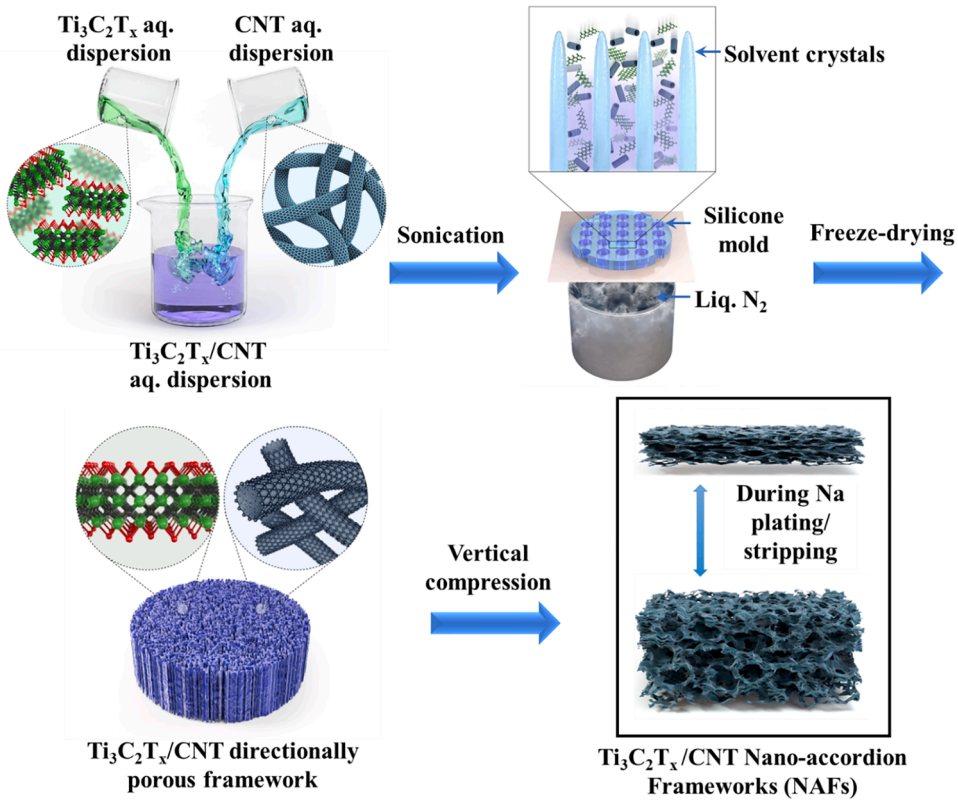

Scheme 1. Schematic illustration of the synthesis of resilient $Ti_3C_2T_x$/CNT NAFs.

revealing a structure comprising vertically aligned 2D micro-cellular separated by significant interstitial micro-sized pores. The micro-size porous spacing between each cellular framework is around 20 μm. Fig. 1c exhibits evenly dispersed CNTs on the surface and within the interstices of the 2D $Ti_3C_2T_x$ layers. As a result of their high conductivity and mechanical robustness, the CNTs in $Ti_3C_2T_x$/CNT NAFs can effectively maintain the structure even after repeated plating and stripping (Fig. S3). The top-view SEM image of pressed $Ti_3C_2T_x$/CNT NAFs on a Cu foil (Fig. 1d) exhibiting a similar structure to that of the as-prepared top-view SEM image (Fig. 1a), which reveals that the original alignment and porous structure were still maintained in the pressed $Ti_3C_2T_x$/CNT NAFs. Compressed $Ti_3C_2T_x$/CNT NAFs on a Cu foil were cut with an ion milling system, and their cross-sectional morphology was then analyzed. Vertically pressed $Ti_3C_2T_x$/CNT NAFs on Cu foil showed an accordion-like structure [46], maintaining their pore channel without restack and structure collapse because of significant space between each $Ti_3C_2T_x$/CNT NAFs layer (Fig. 1e). This nano-accordion structure with easy vertical deformation can effectively accommodate volume changes during repeated long-term plating and stripping, resulting in an improved average CE throughout the cycling. The color mapping of the $Ti_3C_2T_x$/CNT NAFs on a Cu foil reveals the presence of Ti and C as well as O and F surface functional groups (Fig. 1f).

Fig. 1g depicts the Raman spectra of pure $Ti_3C_2T_x$ film and $Ti_3C_2T_x$/CNT NAF samples. Pure $Ti_3C_2T_x$ film has a resonant peak at 156 cm^{-1}[47] and other Raman vibrations at 201 (ω_2), 275 (ω_5), 380 (ω_5), 520 (ω_4), 626 (ω_4), and 717 cm^{-1} (ω_3); however, they can only be observed in $Ti_3C_2T_x$/CNT NAFs at 201 (ω_2), 380 (ω_5), 520 (ω_4), and 626 cm^{-1} (ω_4). The vibrations of ω_2 and ω_3 are associated with the out-of-plane vibrations of the Ti and C atoms with A_{1g} symmetry [48]. The vibrations of ω_4 and ω_5 include shear modes of in-plane vibrations of Ti and C atoms and surface functional groups, which are all associated with E_g symmetry [48]. CNTs are known to exhibit radial breathing mode (RBM)[49] and are found in $Ti_3C_2T_x$/CNT NAFs at 152.5, 180, 250, and 269 cm^{-1}, corresponding to CNTs tube diameters of 1.63, 1.38, 0.99, and 0.92 nm. $Ti_3C_2T_x$/CNT NAFs display additional bands at 1,338 (defect-induced, D), 1,591 (graphitic mode, G), 1,744 (overtone of the oTO mode, M), 2,668 (overtone of the D mode, G'), and 3,177 cm^{-1} (overtone of the G mode, 2G') [49–51]. The high intensity of the G band around 1,591 cm^{-1} suggests a larger concentration of sp^2 hybridized carbon, which is advantageous for enhancing the electrical conductivity of $Ti_3C_2T_x$/CNT NAFs [51]. This Raman spectrum indicates the existence of $Ti_3C_2T_x$ and CNTs within $Ti_3C_2T_x$/CNT NAFs.

We have utilized X-ray photoelectron spectroscopy (XPS) to examine the chemical states and terminal surface functional groups in $Ti_3C_2T_x$/CNT NAFs. Fig. 1h displays the XPS survey spectrum, confirming the existence of Ti, C, O, and F in $Ti_3C_2T_x$/CNT NAFs. The Ti 2p high-resolution XPS spectrum displays three doublets of asymmetric peaks centered at 455.2 eV (461.3 eV), 456.1 eV (462.2 eV), and 457.2 eV (463.3 eV) with an energy difference (ΔE) of 6.1 eV, related to C−Ti^{+}, C−Ti^{2+}, and C−Ti^{3+}, respectively (Fig. 1i) [52]. These three doublets are attributed to C−Ti−C in the core of the layer and Ti atoms coupled to C atoms and terminal surface functional groups including C−Ti−O, C−Ti−OH, and C−Ti−F in $Ti_3C_2T_x$ of $Ti_3C_2T_x$/CNT NAFs [53]. Two further doublets, centered at 459.0 (464.1) and 459.9 (465.1) eV, are attributed to $TiO_{2-x}F_{2x}$ and TiF_x, respectively [53]. The high-resolution XPS spectrum of C 1s reveals five peaks centered at 281.8, 283.0, 284.4, 285.8, and 288.3 eV, which are related to C−Ti, C−Ti−T_x, C−, C−O, and C=O/C−F, respectively (Fig. 1j) [54]. The O 1s high-resolution XPS spectrum displays six peaks centered at 529.7, 530.2, 531.0, 531.9, 533.0, and 534.0 eV, which are attributed to C−Ti−O(i), $TiO_{2-x}F_{2x}$, C−Ti−O(ii), C−Ti−OH, OR, and H_2O, respectively (Fig. 1k) [52]. The high-resolution XPS spectrum of F 1s exhibits two peaks centered at 684.9 and 686.5 eV, attributed to C−Ti−F_x and $TiO_{2-x}F_{2x}$, respectively (Fig. 1l) [52]. The XPS results demonstrate the presence of various surface oxidation states and surface terminal functional groups in the $Ti_3C_2T_x$/CNT NAFs.

Pristine Cu foil, $Ti_3C_2T_x$ NAFs, CNT FSEs, $Ti_3C_2T_x$ film, and $Ti_3C_2T_x$/CNT NAFs ($Ti_3C_2T_x$:CNT = 7:3, 8:2 & 9:1) were tested for their

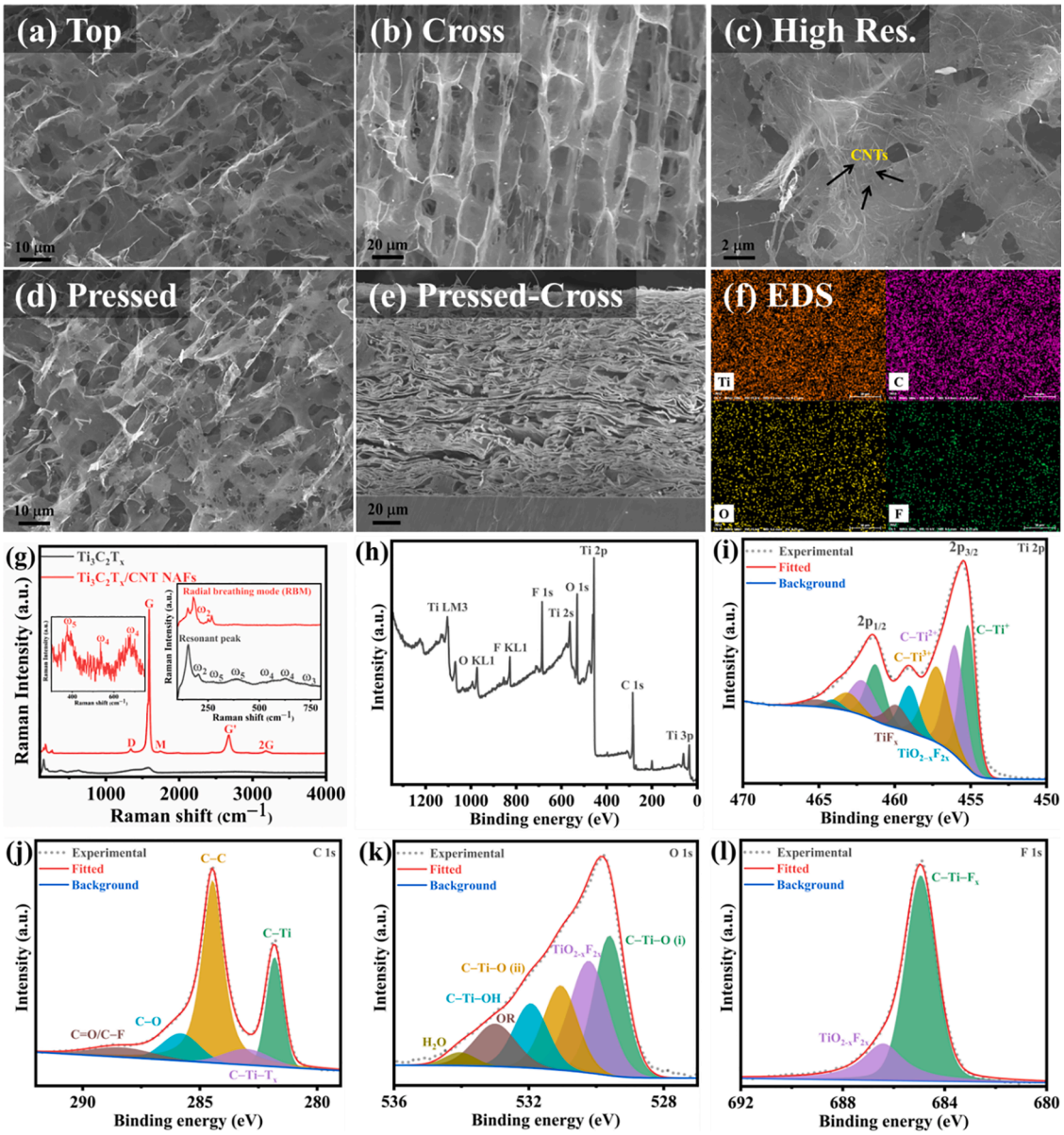

Fig. 1. (a) Top-view FE-SEM images of as-prepared $Ti_3C_2T_x$/CNT NAFs at low magnification. (b) Cross-sectional FE-SEM image of as-prepared $Ti_3C_2T_x$/CNT NAFs. (c) High magnification FE-SEM image of as-prepared $Ti_3C_2T_x$/CNT NAFs. (d and e) Top-view and cross-sectional-view FE-SEM images of pressed $Ti_3C_2T_x$/CNT NAFs on a Cu foil. (f) EDS color mapping of $Ti_3C_2T_x$/CNT NAFs in a top-view. (g) Raman spectra of $Ti_3C_2T_x$ film and $Ti_3C_2T_x$/CNT NAF samples; insets show the enlarged ranges. (h) XPS survey spectrum and high-resolution XPS spectrums of the (i) Ti 2p, (j) C 1s, (k) O1s, and (l) F1s of the $Ti_3C_2T_x$/CNT NAF sample.

sodiophilic activity in 1.0 M sodium hexafluorophosphate ($NaPF_6$) in diglyme (DGM) at a capacity of 1.0 mAh cm^{-2} at 1.0 mA cm^{-2}. All these cells were precycled between 0.01 and 1.0 V *vs.* Na/Na^+ at a current of 100.0 μA cm^{-2} before performing Na nucleation on these substrates; the resulting plot of $Ti_3C_2T_x$/CNT NAFs/Na (8:2) is shown in Fig. S4a. With $Ti_3C_2T_x$:CNT ratio of 8:2, better electrochemical performance is achieved (detailed in the supplementary data, Fig. S4b–d), and subsequent experiments were conducted using this sample. The initial Na nucleation overpotentials might provide insights into the sodiophilicity of various substrates [11,40] The overpotentials are calculated to be 38.5, 10.6, 12.4, 40.6 mV and 9.0 mV for pristine Cu foil, $Ti_3C_2T_x$ NAFs, CNT FSEs, $Ti_3C_2T_x$ film, and $Ti_3C_2T_x$/CNT NAFs, respectively (Fig. 2a). $Ti_3C_2T_x$/CNT NAFs have the lowest overpotential among the five substrates, indicating the lowest Na nucleation energy barrier and uniform Na nucleation sites across the entire surface and interstices. This is because of synergistically improved chemical affinity by the $Ti_3C_2T_x$/CNT NAFs for faster Na^+/electron (e^-) transport across the whole surface and interstices. Given the dramatic improvement in nucleation overpotential when the morphology of the electrode changes from film to NAFs in the case of $Ti_3C_2T_x$ alone, it can be inferred that the intrinsic sodiophilicity of $Ti_3C_2T_x$ is quite high. Moreover, this confirms that the scale and structure of the electrode/electrolyte interface are crucial factors in determining nucleation performance. $Ti_3C_2T_x$ NAFs and CNT FSEs had slightly higher overpotentials to $Ti_3C_2T_x$/CNT NAFs, indicating the sodiophilic characters; however, due to the easily breakable nature of $Ti_3C_2T_x$ NAFs, we were unable to use for additional electrochemical tests. In contrast, the overpotentials of $Ti_3C_2T_x$ film and pristine Cu foil are approximately four times higher than the others. This could be due to Cu foils and especially structurally inferior $Ti_3C_2T_x$ films forming heterogeneous Na nucleation sites and thermodynamically incompatible surfaces with the Na metal [40]

Fig. 2b displays the voltage plot of Na plating and stripping of five substrates with a capacity of 1.0 mAh cm^{-2} at 1.0 mA cm^{-2}. Pristine Cu foil, $Ti_3C_2T_x$ NAFs, CNT FSEs, and $Ti_3C_2T_x$ films have the highest voltage

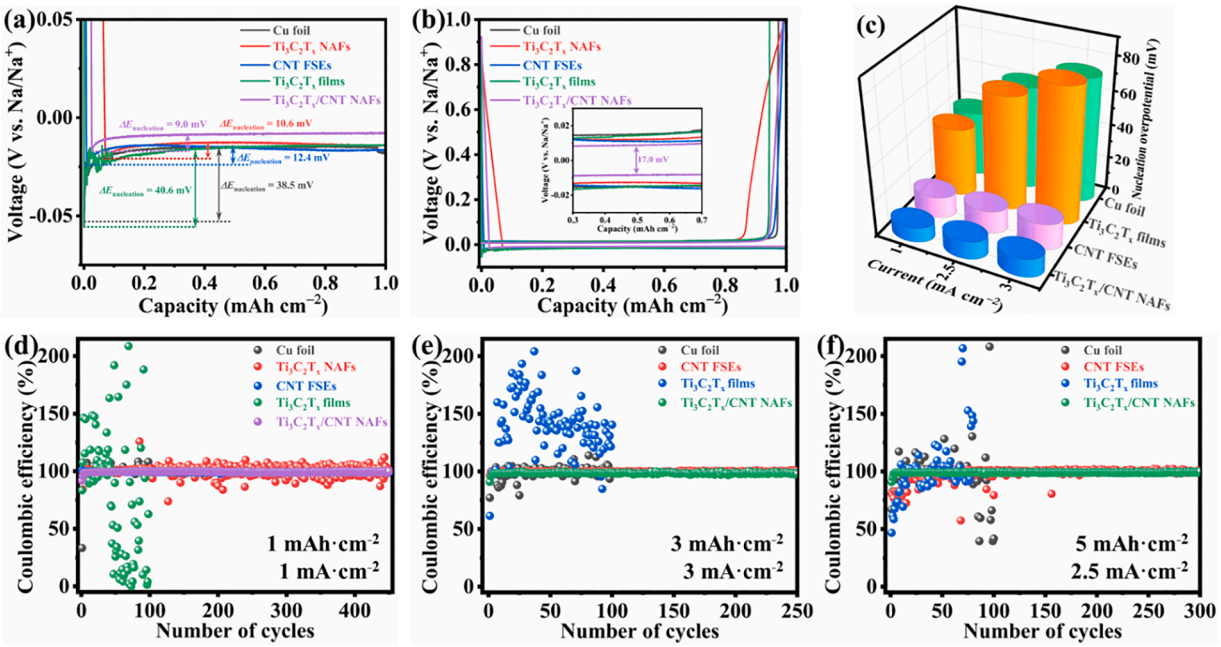

Fig. 2. (a) Nucleation overpotential and (b) Na plating and stripping plots of pristine Cu foil, $Ti_3C_2T_x$ NAFs, CNT FSEs, $Ti_3C_2T_x$ film, and $Ti_3C_2T_x$/CNT NAFs with a capacity of 1.0 mAh cm^{-2} at 1.0 mA cm^{-2}; inset shows the enlarged voltage *vs.* capacity profiles. (c) Nucleation overpotential as a function of the current plot of pristine Cu foil, $Ti_3C_2T_x$ film, CNT FSEs, and $Ti_3C_2T_x$/CNT NAFs. CE plots of pristine Cu foil, CNT FSEs, $Ti_3C_2T_x$ film, and $Ti_3C_2T_x$/CNT NAFs with varying capacities and currents of (d) 1.0 mAh cm^{-2} at 1.0 mA cm^{-2}, (e) 3.0 mAh cm^{-2} at 3.0 mA cm^{-2}, and (f) 5.0 mAh cm^{-2} at 2.5 mA cm^{-2}.

hysteresis of 29.6, 24.7, 26.5, and 29.4 mV, respectively, while $Ti_3C_2T_x$/CNT NAFs have a voltage hysteresis of just 17.0 mV. We then estimated the nucleation overpotential with varying capacities of 1.0 to 5.0 mAh cm^{-2} at different currents of 1.0 to 3.0 mA cm^{-2} on these four substrates, and the findings are displayed in Fig. 2c. In response to an increase in current from 1.0 to 3.0 mA cm^{-2}, the nucleation overpotential of pristine CNT FSEs increases slightly from 12.4 to 15.4 mV, suggesting uniform Na nucleation-guided nature of CNT FSEs. Similar to CNT FSEs, the nucleation overpotential of $Ti_3C_2T_x$/CNT NAFs increases just slightly from 9.0 to 10.8 mV. In contrast, the nucleation overpotentials of pristine Cu foil (38.5 to 73.4 mV) and $Ti_3C_2T_x$ films (40.6 to 80.2 mV) increase rapidly. The lower voltage hysteresis and overpotential in $Ti_3C_2T_x$/CNT NAFs can be related to the homogeneous distribution of Na nucleation sites and reduced local current at the interface through outstanding sodiophilicity [10], both of which favor the formation of stable SEI containing NaF, thus performing uniform long-term plating and stripping [15].

Any substrate can make a stable SEI after some cycles of plating and stripping in the electrolyte. For the precise determination of CE, a stabilization process is required, and after that, any further loss of Na metal must be attributed to the reaction between the electrolyte and Na metal on the substrate, such as chemical corrosion [55]. In the $Ti_3C_2T_x$/CNT NAFs/Na asymmetric cell, the average CE was determined by plating a charge of 5.0 mAh cm^{-2} and then completely stripping the cell to 1.0 V. Then, the 5.0 mAh cm^{-2} Na reservoir (Q_T) was plated at 1.0 mA cm^{-2}, subjected to ten cycles of stripping and plating at a 1.0 mAh cm^{-2} capacity (Q_C), and then stripped (Q_S) to 1.0 V at 1.0 mA cm^{-2} (Fig. S4e). The following equation can be used to approximate the mean CE of an asymmetric $Ti_3C_2T_x$/CNT NAFs/Na cell [55].

$$CE_{Avg} = \frac{nQ_C + Q_S}{nQ_C + Q_T} \times 100 \quad (1)$$

Here, the average CE is evaluated without considering the first cycle of substrate preconditioning, and it was found to be 99.8 %, indicating that $Ti_3C_2T_x$/CNT NAFs are capable of high-quality Na plating and stripping. The CE plots for four substrates with capacities of 1.0, 3.0, and 5.0 mAh cm^{-2} at different currents of 1.0, 3.0, and 2.5 mA cm^{-2} are depicted in Fig. 2d–f. The average CEs of pure CNT FSEs/Na asymmetric cells are calculated to be 99.5 % (1.0 mAh cm^{-2} at 1.0 mA cm^{-2}, 600 h) and 99.3 % (3.0 mAh cm^{-2} at 3.0 mA cm^{-2}, 500 h), but the CE at 5.0 mAh cm^{-2} at 2.5 mA cm^{-2} fluctuates abruptly, signifying the formation of hotspots (Fig. 2f), suggesting incompatible hosting nature beyond Na capacity of 3.0 mAh cm^{-2}. A pristine Cu foil/Na asymmetric cell showed that the corrosion of the pristine Cu foil in the presence of electrolyte probably contributed to the failure of the cell after a few cycles. Pure $Ti_3C_2T_x$ film has a compact dense structure limiting the availability of Na nucleation sites [46], causing hotspots during plating and stripping cycles and mossy dendrites, resulting in a significant fluctuation in CE [29]. $Ti_3C_2T_x$/CNT NAFs/Na asymmetric cell achieves CEs of over 99.0 % in the first five cycles across a wide range of capacities and currents. The average CEs of $Ti_3C_2T_x$/CNT NAFs/Na asymmetric cells are reported to be 99.7 % (1.0 mAh cm^{-2} at 1.0 mA cm^{-2}, 900 h), 99.5 % (3.0 mAh cm^{-2} at 3.0 mA cm^{-2}, 500 h), and 99.0 % (5.0 mAh cm^{-2} at 2.5 mA cm^{-2}, 1,200 h). The asymmetric $Ti_3C_2T_x$/CNT NAFs/Na cells exhibited superior CEs relative to previously reported $Ti_3C_2T_x$-based asymmetric cells (Table S1). These results suggest that $Ti_3C_2T_x$/CNT NAFs have extraordinary sodiophilicity and well-maintained directionally porous channels despite being pressed, which promote the easy infiltration of electrolytes and also shorten the transit of Na^+/electrons into the interstices of their host structure [11]. Moreover, because of the resilient effect during Na plating/stripping, the vertically deformable nano-accordion structures can adapt to volume variation, as a result, exceptional CE is maintained during the prolonged plating and stripping process [9].

Afterward, we plated 3.0 mAh cm^{-2} Na capacity at 3.0 mA cm^{-2} on pristine Cu foil, $Ti_3C_2T_x$ film, CNT FSEs, and $Ti_3C_2T_x$/CNT NAFs and examined their surface morphology with FE-SEM after the first and fifty cycles to corroborate the surface characteristics of Na plating in these substrates (Fig. S5). One plating cycle on pristine Cu foil resulted in uneven deposition of Na and numerous surface fractures (Fig. S5a). After fifty cycles, the surface of pristine Cu foil becomes much rougher and more cracked (Fig. S5e). The first cycle reveals Na deposition on the surface of $Ti_3C_2T_x$ film, as well as the uneven distribution of numerous tiny Na dendrites (Fig. S5b). The CNT FSEs show uniform Na deposition

without dendrites at first (Fig. S5c) and after the fiftieth cycle (Fig. S5g), suggesting the sodiophilic nature of CNT FSEs. Similar to CNT FSEs, $Ti_3C_2T_x$/CNT NAFs demonstrate homogenous Na deposition on their surface from the initial first cycle (Fig. S5d) and after fifty cycles (Fig. S5h). Their micron-sized porous surface structure remains intact even after fifty cycles, which is advantageous for both electrolyte accessibility to the internal host structure and quicken Na^+/electron tunneling at the interface, resulting in long-term plating and stripping with sustained CE.

To understand the various SEI components on the surface of $Ti_3C_2T_x$/CNT NAFs, we analyzed the surface of $Ti_3C_2T_x$/CNT NAFs after 50 cycles of plating and stripping using XPS, and the relevant findings are presented in Fig. S6. After the Na plating, the Ti 2p peaks shift to lower binding energies, indicating a partial reduction of Ti (Fig. S6b) [15]. The high-resolution C 1s spectrum shows the presence of organic and inorganic components in SEI, including C−O (R−O−R), C−O (R−O−Na), C=O, and C=O (R−CO_2−Na) (Fig. S6c) [56]. The presence of Na−O and Na−F is suggested by the high-resolution spectrum of O 1s (Fig. S6d) [57]. The high-resolution F 1s spectrum reveals the presence of Na−F, P−O−F_x, and Na_x−P−F_y in SEI (Fig. S6e) [56]. The high-resolution Na 1s spectrum further confirms the formation of Na−O, Na−C, and Na−F (Fig. S6f) [57]. These findings suggest the formation of stable SEI with various sodium- and fluorine-based organic and inorganic components on the surface of $Ti_3C_2T_x$/CNT NAFs during cycling, which can speed up Na^+/electron (e^-) tunneling at the interface without dendrite formation, resulting in sustained CE during long-term plating and stripping.

To gain a better understanding of the electrochemical Na plating and stripping processes in $Ti_3C_2T_x$/CNT NAFs, we deposited Na at various capacities ranging from 1.0 to 5.0 mAh cm^{-2} at a current of 1.0 mA cm^{-2} and stripped it to 3.0 mAh cm^{-2} and finally to 1.0 V at the same current. By measuring the top-view and cross-sectional view of Na-deposited and -stripped samples, the sodiophilicity and stability of $Ti_3C_2T_x$/CNT NAFs

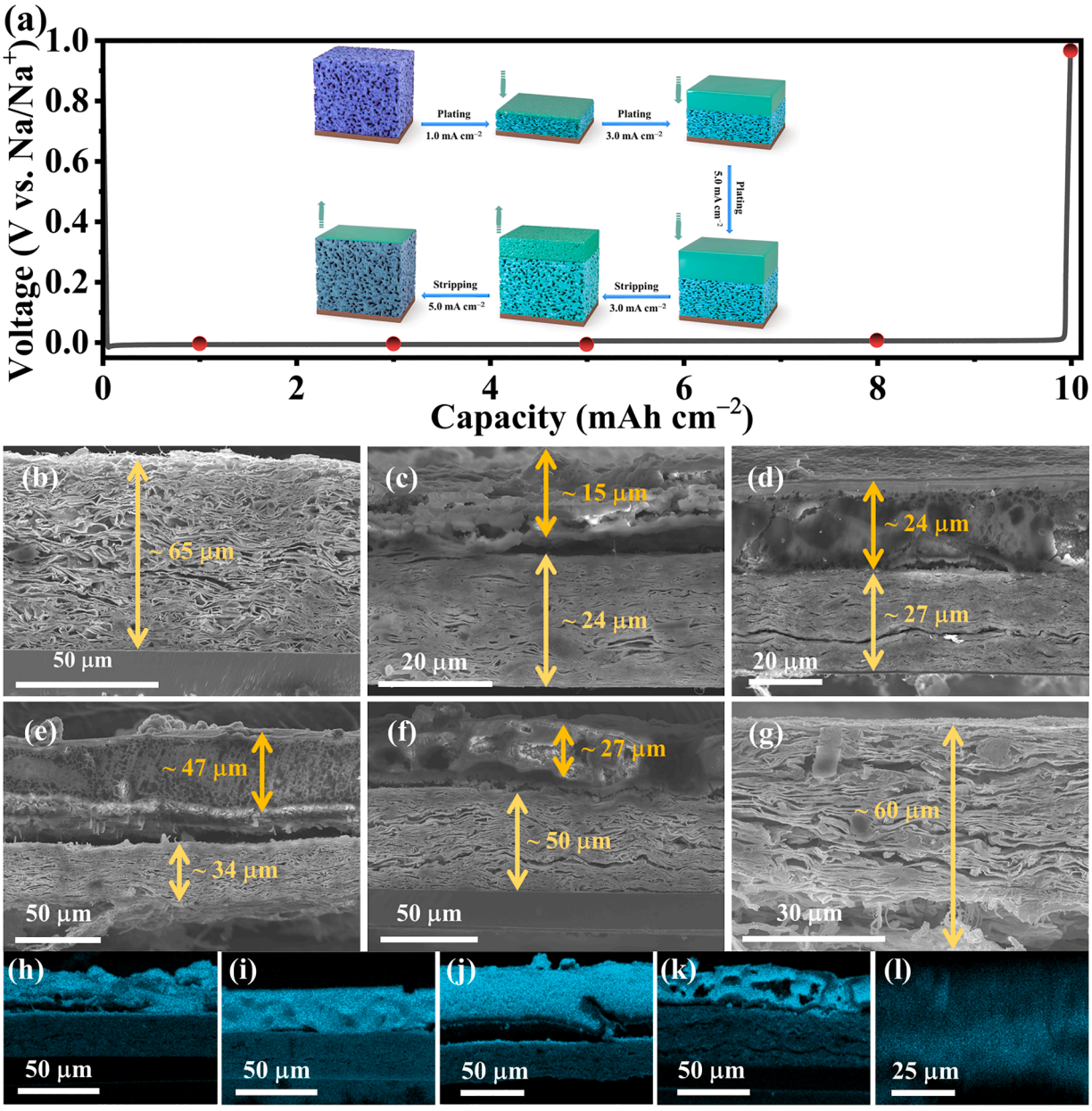

Fig. 3. (a) Na plating and stripping states marked in voltage *vs.* capacity plot at 1.0 mA cm^{-2} in each step; inset shows a schematic depiction of Na platting and stripping behavior in the $Ti_3C_2T_x$/CNT NAFs at various states. Cross-sectional-view FE-SEM images of $Ti_3C_2T_x$/CNT NAFs at (b) fresh state, plating at (c) 1.0 mAh cm^{-2}, (d) 3.0 mAh cm^{-2}, (e) 5.0 mAh cm^{-2}, and stripping to (f) 3.0 mAh cm^{-2}, and (g) stripping to 1.0 V *vs.* Na/Na^+. (h–l) Na EDS color mappings of plating and stripping states of $Ti_3C_2T_x$/CNT NAFs.

can be determined. Figs. 3 and S7 show cross-sectional and top-view FE-SEM images of Na-deposited and -stripped samples, respectively. The inset of Fig. 3a depicts a schematic representation of the Na plating and stripping processes that occur in $Ti_3C_2T_x$/CNT NAFs in each step. Fig. 3b shows a cross-sectional FE-SEM image of $Ti_3C_2T_x$/CNT NAFs uncoated Na with a nano-accordion structure with a thickness of approximately 65 μm. $Ti_3C_2T_x$/CNT NAFs with a Na deposition capacity of 1.0 mAh cm^{-2} show that Na has been infused between the $Ti_3C_2T_x$/CNT NAFs interstices and on their top surface (Fig. 3c). Fascinatingly, after Na deposition, the thickness of the nano-accordion structure of $Ti_3C_2T_x$/CNT NAFs shrunk from around 65 μm to approximately 24 μm, while the thickness of Na over the surface was measured to be about 15 μm. The EDS picture in Fig. 3h shows that Na is present within the nano-accordion structure and on their surface. Since the Na is simultaneously deposited on the inside of the nano-accordion structure of $Ti_3C_2T_x$/CNT NAFs and their surface, the porous inter-connected channels within the NAFs contract due to the capillary effect from the Na metal particles deposited inside the pore. The contraction of the NAFs is quite homogeneous spatially, resulting in the top surface of the electrode retaining a macroscopically flat (Fig. S7a) but microscopically rough surface (Fig. S7b). At a plating capacity of 3.0 mAh cm^{-2}, top-view FE-SEM images indicate uniform and flat Na deposition on the surface of $Ti_3C_2T_x$/CNT NAFs (Fig. S7d and e). The cross-sectional FE-SEM image reveals a slightly increased thickness of $Ti_3C_2T_x$/CNT NAFs, from 24 μm to 27 μm, as well as a homogeneously uniform layer of Na on top of the $Ti_3C_2T_x$/CNT NAFs with a thickness of around 24 μm (Fig. 3d). EDS color mapping demonstrates that the Na concentration is greater on the top surface than in the interstices of $Ti_3C_2T_x$/CNT NAFs (Fig. 3i). With an increase in Na deposition from 3.0 to 5.0 mAh cm^{-2}, the top-view FE-SEM images exhibit the same characteristics (Fig. S7g and h) as those obtained at 3.0 mAh cm^{-2}, whereas a cross-sectional FE-SEM image reveals that the thickness of $Ti_3C_2T_x$/CNT NAFs has expanded from 27 μm to 34 μm, and the surface Na thickness has risen to around 47 μm (Fig. 3e). EDS image exhibits vibrant color due to Na at the interstices of $Ti_3C_2T_x$/CNT NAFs and on their surface (Fig. 3j).

After stripping to 3.0 mAh cm^{-2}, cross-sectional (Fig. 3f) and top-view (Fig. S7j and k) FE-SEM images exhibit voids and a rough surface on the top of $Ti_3C_2T_x$/CNT NAFs. The thickness of the $Ti_3C_2T_x$/CNT NAFs is bounced from 34 μm to 50 μm, with substantial micro-sized pores space in the interstices with the residual Na on the top surface of the $Ti_3C_2T_x$/CNT NAFs; the thickness of the Na on top-surface was measured to be around 27 μm. The Na intensity on the EDS image is lowest between the $Ti_3C_2T_x$/CNT NAFs' layers compared to the top surface, where it shines through many voids (Fig. 3k). It is considered that stripping occurs at the interstitial part first because of the lower overpotential followed by from the top of the Na layer. After Na was completely stripped to 5.0 mAh cm^{-2}, top-view FE-SEM images reveal a trace of Na on the surface, along with some porous structures (Fig. S7m and n). The cross-sectional FE-SEM image shows the well-maintained nano-accordion structure with a thickness of around 60 μm without structure collapse (Fig. 3g). It is mainly due to the high mechanical deformability of $Ti_3C_2T_x$/CNT NAFs. Na has been successfully stripped from the interstices of the $Ti_3C_2T_x$/CNT NAFs, as evidenced by the EDS mapping, which reveals a small amount of Na well-distributed on the layers of $Ti_3C_2T_x$/CNT NAFs (Fig. 3l). $Ti_3C_2T_x$/CNT NAFs still contained Ti, C, O, F, Na, and P during the plating and stripping. This was

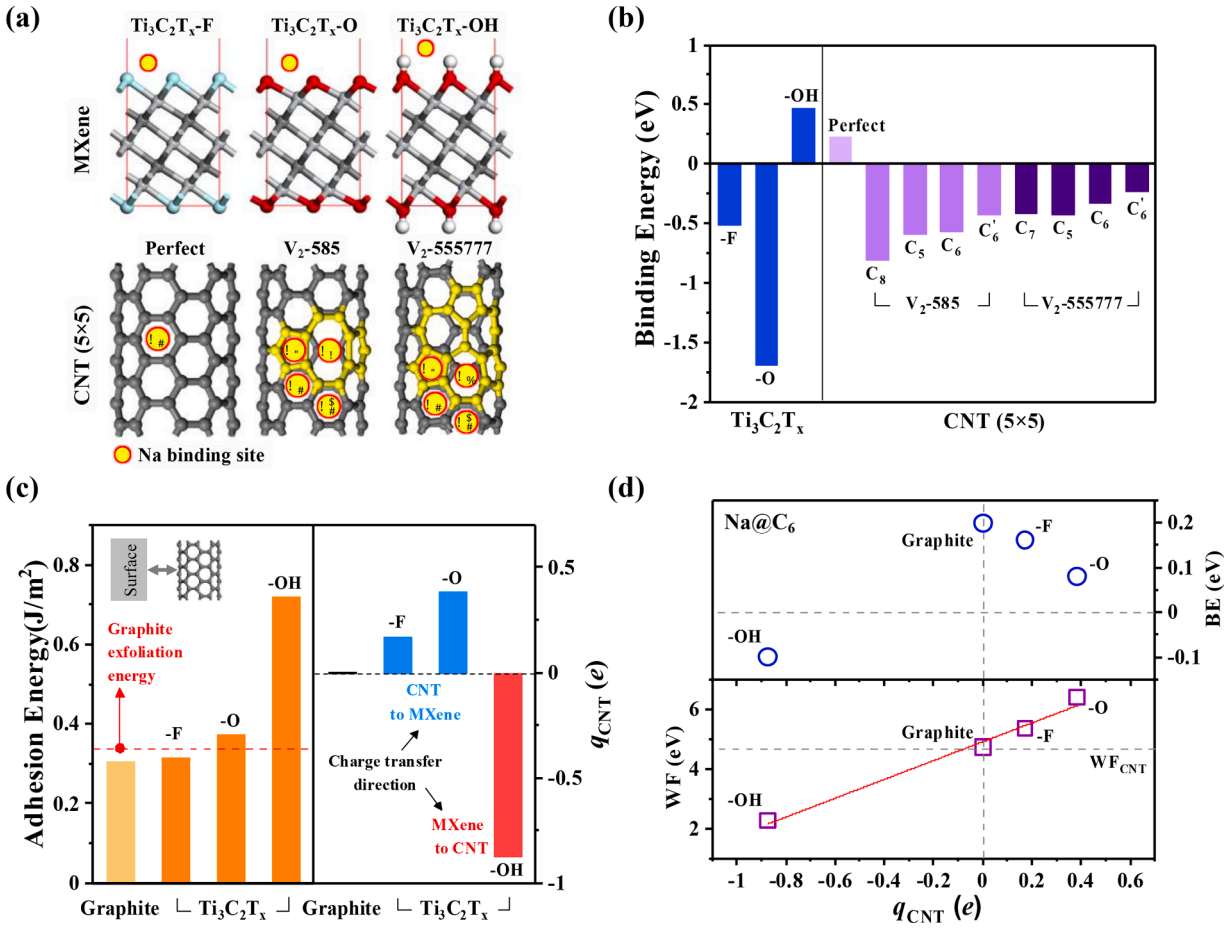

Fig. 4. (a) Structures for three types of surface termination of MXene and CNT with and without topological defects. (b) Calculated binding energies of Na on the $Ti_3C_2T_x$ and CNT surfaces. (c) Calculated adhesion energies for the junction between CNT and $Ti_3C_2T_x$ surfaces, as well as the sum of the partial charge of CNT. (d) Relationship between charge transfer, work function, and Na binding energy.

corroborated by top-view EDS mapping (Fig. S7c, f, l, and o) and cross-sectional EDS mapping (Fig. S8). These findings prove that resilient $Ti_3C_2T_x$/CNT NAFs nano-accordion structures durably and reversibly possess Na accommodation sites with high sodiophilicity with little total volume changes during the plating/stripping process.

Atomic-level analyses of experimental results were conducted using first-principles calculations. First, the intrinsic sodiophilicity of MXene and CNT was calculated for $Ti_3C_2T_x$ surfaces fully terminated with −F, −O, and −OH, as well as 5 × 5 CNT surfaces both with and without topological divacancy defects (Fig. 4a). As shown in Fig. 4b, the $Ti_3C_2T_x$ surfaces terminated with −F and −O exhibit strong sodiophilicity, displaying binding energies of −0.51 and −1.69 eV, respectively. In contrast, the surface terminated with −OH does not interact with sodium, presenting a binding energy of +0.47 eV. Considering that the reference energy for the Na atom used in the binding energy calculation is equivalent to Na metal, the binding energy value can be converted into the reduction potential of Na^+ with respect to the Na/Na^+ electrode potential by multiplying it by −1. This implies that the electrochemical reduction of Na^+ proceeds rapidly at a high positive potential on −F and −O termination sites (0.51 and 1.69 V vs. Na/Na^+, respectively), serving as effective nucleation sites, unlike the −OH terminated site. However, as the actual $Ti_3C_2T_x$ material has these functional groups distributed randomly on its surface, various Na^+ reduction potentials could be exhibited depending on the configuration. This may account for the large sloping capacity observed in the $Ti_3C_2T_x$ NAFs electrode. Furthermore, considering the operating potential range of the anode in the experiment, it is highly probable that adsorbed Na atoms on the −F dominated surface will not oxidize into Na^+ due to its strong sodiophilicity, which could influence the initial CE.

For the CNT surface, there is a noticeable correlation between Na binding and the presence of defects. When examining a perfect CNT, the C_6 ring exhibits a binding energy of +0.23 eV, which does not favor binding. However, introducing two types of divacancies (V_2−585 and V_2−555777 depicted in Fig. 4a) significantly increases the sodiophilicity not only at the C_8, C_7, and C_5 defect sites but also at the adjacent C_6 and C_6' sites, bringing the binding energy down to a range of −0.23 to −0.80 eV (as shown in Fig. 4b). This pattern is consistent with findings from previous studies: defects amplify the density of states near the Fermi level, which in turn boosts the electron affinity of the surface, facilitating stronger Coulomb interactions with adsorbed Na atoms [58]. Consequently, the notably low nucleation overpotential observed in the CNT FSEs electrode during the experiment is likely due to the variety of topological defects present on the CNT surface. Given the inherent sodiophilicity of both the $Ti_3C_2T_x$ and CNT surfaces, the $Ti_3C_2T_x$/CNT NAFs electrode is also believed to have a substantial number of effective sodiophilic sites.

Next, potential physicochemical synergetic effects arising from the interaction between $Ti_3C_2T_x$ and CNT within the NAFs composite electrode were examined. Additional calculations were carried out on structures bridging CNT and $Ti_3C_2T_x$ surfaces with different functional groups (refer to the inset of Fig. 4c). For comparison purposes, a model with a pure van der Waals (vdW) junction between graphite and CNT was also included. As depicted in the left part of Fig. 4c, the adhesion energy between a perfect CNT and a graphite surface amounts to 0.31 J/m^2, closely resembling the experimental graphite exfoliation energy of 0.34 J/m^2 [59]. Significant differences are observed among the $Ti_3C_2T_x$ surfaces depending on the functional group. Surfaces terminated with −F and −O display adhesion energies of 0.32 and 0.38 J/m^2, respectively, pointing to adhesion principally driven by vdW interactions, akin to the graphite case. Conversely, surfaces terminated with −OH exhibit a considerably stronger interaction, with an adhesion energy of 0.72 J/m^2. This trend suggests that −OH functional groups dispersed on the $Ti_3C_2T_x$ surface likely play a pivotal role in firmly attaching to the CNT. Such robust attachment presumably enables the mechanically resilient NAF structure to preserve its configuration despite repeated expansion and contraction during numerous charge and discharge cycles. Moreover, considering the observed low sodiophilicity of the −OH dominated surface, it can be posited that the count of nucleation sites on the $Ti_3C_2T_x$ surface remains largely unchanged post-junction formation with CNT and may increase due to the additional nucleation sites provided by the CNT.

An analysis of the electronic structure of the junction structure uncovers that, unlike the interaction with the graphite surface, charge transfer can occur when the $Ti_3C_2T_x$ surface is implicated, and this process hinges on the type of surface functional groups. A calculation of the sum of the partial charge of CNT (q_{CNT}) reveals that the −F and −O surfaces extract electrons from the CNT, with resulting q_{CNT} values are +0.17 and +0.38 *e*, respectively. In contrast, the −OH surface facilitates the transfer of electrons from the surface to the CNT, resulting in a q_{CNT} value is −0.38 *e* (right part of Fig. 4c). These outcomes can be lucidly explained by the work function (WF) discrepancy between the CNT and the surface. Surfaces with a higher WF than CNT are likely to uptake electrons from the CNT, while those with a lower WF tend to inject electrons into the CNT (bottom part of Fig. 4d). Moreover, this charge transfer behavior exerts an influence on the Na binding energy. Regardless of the charge transfer direction, an increase in charging causes the Na binding energy of the perfect CNT to escalate (top part of Fig. 4d). This mechanism may also instigate an additional improvement in sodiophilicity at the CNT defect sites. However, the real $Ti_3C_2T_x$ surface is not likely to exhibit such a drastically biased surface state as the calculation model, so the changes may not be as extreme as the calculations suggest. Nonetheless, these synergistic effects of CNT charging and the enhancement of sodiophilicity could be potential explanations for the additional performance improvements observed experimentally in the composite $Ti_3C_2T_x$/CNT NAFs electrode.

Figs. 5 and S9 depict the outcomes of an examination into the interfacial stability of symmetrical cells, including $Ti_3C_2T_x$/CNT NAFs//$Ti_3C_2T_x$/CNT NAFs (Fig. 5) and Na//Na, CNT FSEs//CNT FSEs, and $Ti_3C_2T_x$ film//$Ti_3C_2T_x$ film (Fig. S9) with differing capacities and currents. Initially, the $Ti_3C_2T_x$/CNT NAFs symmetric cell exhibits a very low overpotential of approximately 10.0 mV at a capacity of 3.0 mAh cm^{-2} at 3.0 mA cm^{-2}; after 1,500 h, the overpotential increases slightly to 12.0 mV, indicating exceptional cyclic stability of $Ti_3C_2T_x$/CNT NAFs (Fig. 5a). In contrast, CNT FSEs and $Ti_3C_2T_x$ film symmetric cells exhibit enormous "overpotential bumps", indicating the creation of mossy-type dendrites on the surface, resulting in the occurrence of spatial variation of local reaction kinetics on the electrode surface (Fig. S9a) [11,15]. Na symmetric cell exhibits an overpotential of approximately 7.0 mV at first, however, it abruptly short-circuits after 34 h (Fig. S9a). When subjected to a high current of 10.0 mA cm^{-2} with a capacity of 5.0 mAh cm^{-2}, the $Ti_3C_2T_x$/CNT NAFs symmetric cell exhibits an initial overpotential of around 45.0 mV, which climbs gradually to 58.0 mV after 1,500 h (Fig. 5b). Unfortunately, large overpotential bumps are found in the Na and $Ti_3C_2T_x$ film symmetric cells (Fig. S9b), just as in the prior case of $Ti_3C_2T_x$ film symmetric cells. A $Ti_3C_2T_x$/CNT NAFs symmetric cell with a very high capacity of 20.0 mAh cm^{-2} at 5.0 mA cm^{-2} exhibits an overpotential of approximately 94.0 mV at the beginning, increasing to 100.0 mV after 1,150 h, and then further increasing to about 130.0 mV after 1,200 h (Fig. 5c). In contrast, symmetric cells built from Na and $Ti_3C_2T_x$ film exhibit rising voltage plateaus lasting 110 h for Na and 188 h for $Ti_3C_2T_x$ film before failing (Fig. S9c). It is noted that the $Ti_3C_2T_x$/CNT NAFs symmetric cells outperformed previously reported $Ti_3C_2T_x$-based symmetric cells (Table S2). The rate capabilities of these symmetric cells with a capacity of 3.0 mAh cm^{-2} at a current of 1.0–20.0 mA cm^{-2} were evaluated. Voltage hysteresis in a $Ti_3C_2T_x$/CNT NAFs symmetric cell is relatively constant up to 5.0 mA cm^{-2} and changes slightly at 10.0 and 20.0 mA cm^{-2} (Fig. 5d). Meanwhile, the Na symmetric cell exhibits overpotential bumps at 10.0 and 20.0 mA cm^{-2}. The $Ti_3C_2T_x$ film and CNT FSEs symmetric cells have experienced overpotential bumps at all current densities except 1.0 mA cm^{-2} (Fig. S9d). Electrochemical impedance spectroscopy (EIS) is used to examine the electrode kinetics of the $Ti_3C_2T_x$/CNT NAFs, $Ti_3C_2T_x$ film,

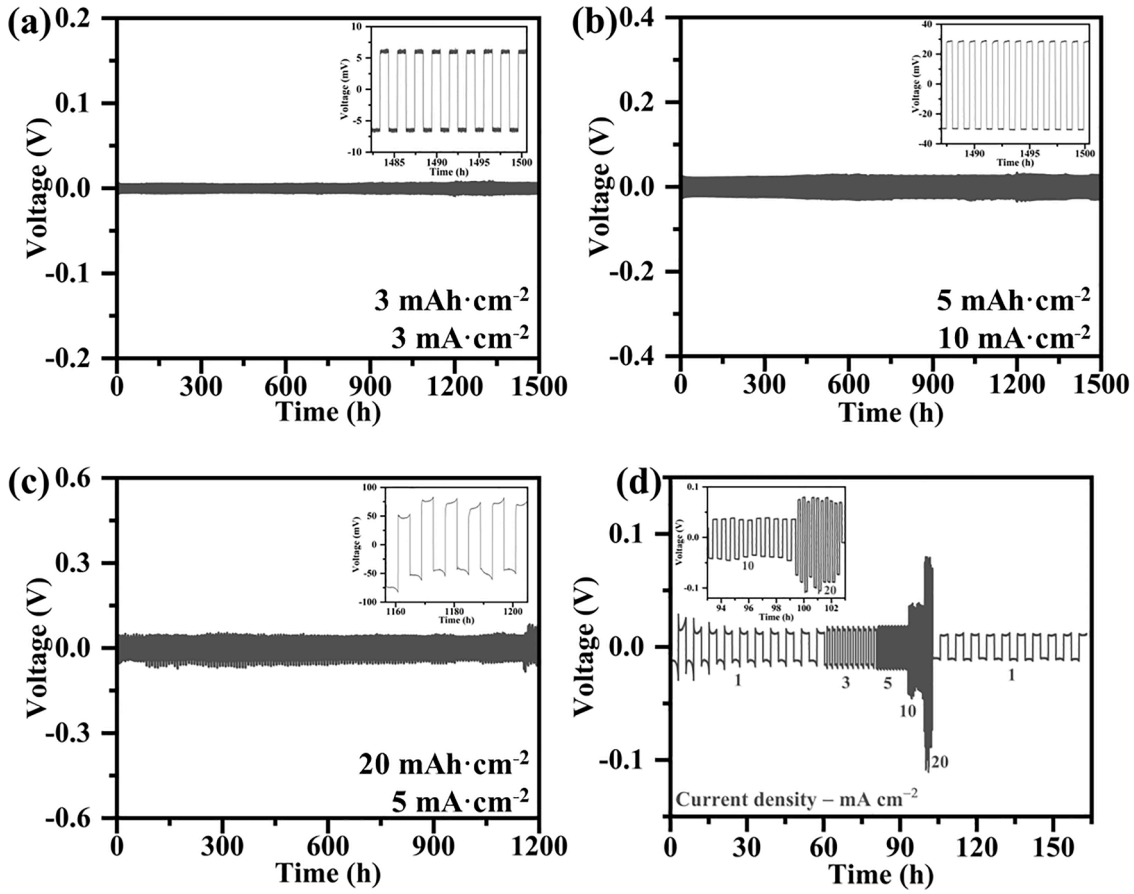

Fig. 5. Electrochemical symmetric cell performance of $Ti_3C_2T_x$/CNT NAFs//$Ti_3C_2T_x$/CNT NAFs at varying capacities and currents of (a) 3.0 mAh cm^{-2} at 3.0 mA cm^{-2}, (b) 5.0 mAh cm^{-2} at 10.0 mA cm^{-2}, and (c) 20.0 mAh cm^{-2} at 5.0 mA cm^{-2}; each inset shows last few cycles. (d) The rate capability of $Ti_3C_2T_x$/CNT NAFs//$Ti_3C_2T_x$/CNT NAFs symmetric cell at a current of 1–20 mA cm^{-2}; inset shows rate performance at 10 and 20 mA cm^{-2}.

and CNT FSEs symmetric cells before and after the fiftieth cycle, and these results are depicted in Fig. S10.

To establish the practical application of $Ti_3C_2T_x$/CNT NAFs as a dendrite-free anode host for AFSMBs, we evaluated the rate capability and cyclic stability of anode-free $Ti_3C_2T_x$/CNT NAFs/Na-SEI//$Na_3V_2(PO_4)_3$@C and Na//$Na_3V_2(PO_4)_3$@C full cells with an industrial scale mass loading of a cathode (~11.0 mg cm^{-2}), and the corresponding outcomes are shown in Figs. 6 and S12. The phase purity of the $Na_3V_2(PO_4)_3$@C sample was confirmed by XRD (Fig. S11a). The FE-SEM image displays the spherical morphology of the $Na_3V_2(PO_4)_3$@C sample, while the EDS color mapping verifies the existence of Na, V, P, and C in the $Na_3V_2(PO_4)_3$@C sample (Fig. S11b and c). Fig. 6a depicts the schematic representation of distinctions between Na-ion, Na-M, and AFSMBs. The anode-free $Ti_3C_2T_x$/CNT NAFs/Na-SEI anode host is fabricated by depositing Na with a capacity of 5.0 mAh cm^{-2} at 1.0 mA cm^{-2} and then stripping it to 0.02 V (Fig. 6b). During the stripping, nearly all of the deposited Na is removed, leaving a small amount of Na with a well-distributed stable SEI on the surface of $Ti_3C_2T_x$/CNT NAFs, which is beneficial for stable cycling when combined with the $Na_3V_2(PO_4)_3$@C cathode; here Na^+ would tunnel from the cathode to the anode and vice versa. It is essential to manage the SEI on the anode and the CEI on the cathode to improve the overall performance of full cells [17]. In light of this, we employ the dual salts ($NaPF_6$ and sodium tetrafluoroborate ($NaBF_4$)) in dimethoxyethane (DME) to regulate the SEI and CEI in our full cells, hence enhancing their performance. The galvanostatic charge-discharge (GCD) curves of the anode-free $Ti_3C_2T_x$/CNT NAFs/Na-SEI//$Na_3V_2(PO_4)_3$@C and Na//$Na_3V_2(PO_4)_3$@C full cells exhibit a stable voltage plateau at 3.4 V *vs.* Na/Na^+ at different C-rate of 0.5, 1.0, 2.0, 5.0 and 10.0 C (Figs. 6c and S12a). After testing the rate capability of these cells, the anode-free $Ti_3C_2T_x$/CNT NAFs/Na-SEI//$Na_3V_2(PO_4)_3$@C cell capacities are determined to be 108.8, 102.1, 96.9, 90.8, and 85.8 mAh g^{-1} at a different C-rate of 0.5, 1.0, 2.0, 5.0, and 10.0 C (Fig. 6d).

One of the key evaluation factors of a cell's longevity is its cyclic stability. Fig. 6e demonstrates that the capacity retention of an anode-free $Ti_3C_2T_x$/CNT NAFs/Na-SEI//$Na_3V_2(PO_4)_3$@C cell at 2.0 C is 69.4 % of its initial cycle capacity after 1,000 cycles, whereas that of Na//$Na_3V_2(PO_4)_3$@C cells is 84.6 %; however, this cell short-circuits in the 1,144th cycle (Fig. S12c). Similarly, the capacity retention of an anode-free $Ti_3C_2T_x$/CNT NAFs/Na-SEI//$Na_3V_2(PO_4)_3$@C cell at 5.0 C is 60.1 % after 1,900 cycles (Fig. 6e), while the capacity retention of Na//$Na_3V_2(PO_4)_3$@C cells is 89.0 %; unfortunately, this cell also fails in the 1,934th cycle (Fig. S12d). However, the anode-free $Ti_3C_2T_x$/CNT NAFs/Na-SEI//$Na_3V_2(PO_4)_3$@C cells retain 53.8 % of their initial capacity at 2.0 C after 2,500 cycles and 43.4 % at 5.0 C after 5,000 cycles. The capacity loss between various cycles is measured for the anode-free $Ti_3C_2T_x$/CNT NAFs/Na-SEI//$Na_3V_2(PO_4)_3$@C cells. At 2.0 C, the capacity loss per cycle is measured to be 0.07, 0.035, 0.019, and 0.010 mAh g^{-1} between 1-100, 101-500, 501-1,000, and 1,001-2,500 cycles, respectively. In similar, at 5.0 C, the capacity loss per cycle is measured to be 0.09, 0.031, 0.013, 0.011, and 0.005 mAh g^{-1} between 1-100, 101-500, 501-1,000, 1,001-2,500, and 2,501-5,000 cycles, respectively. In AFSMBs, Na^+ is transferred solely between the cathode and anode host. Consequently, during the first 1-100 cycles, the creation of a solid electrolyte interface (SEI) occurs on the anode host due to the consumption of little Na^+ from the cathode, resulting in minimal high-capacity loss. Due to the establishment of stable cathode electrolyte interface (CEI) on the cathode and SEI on the anode host, it has been

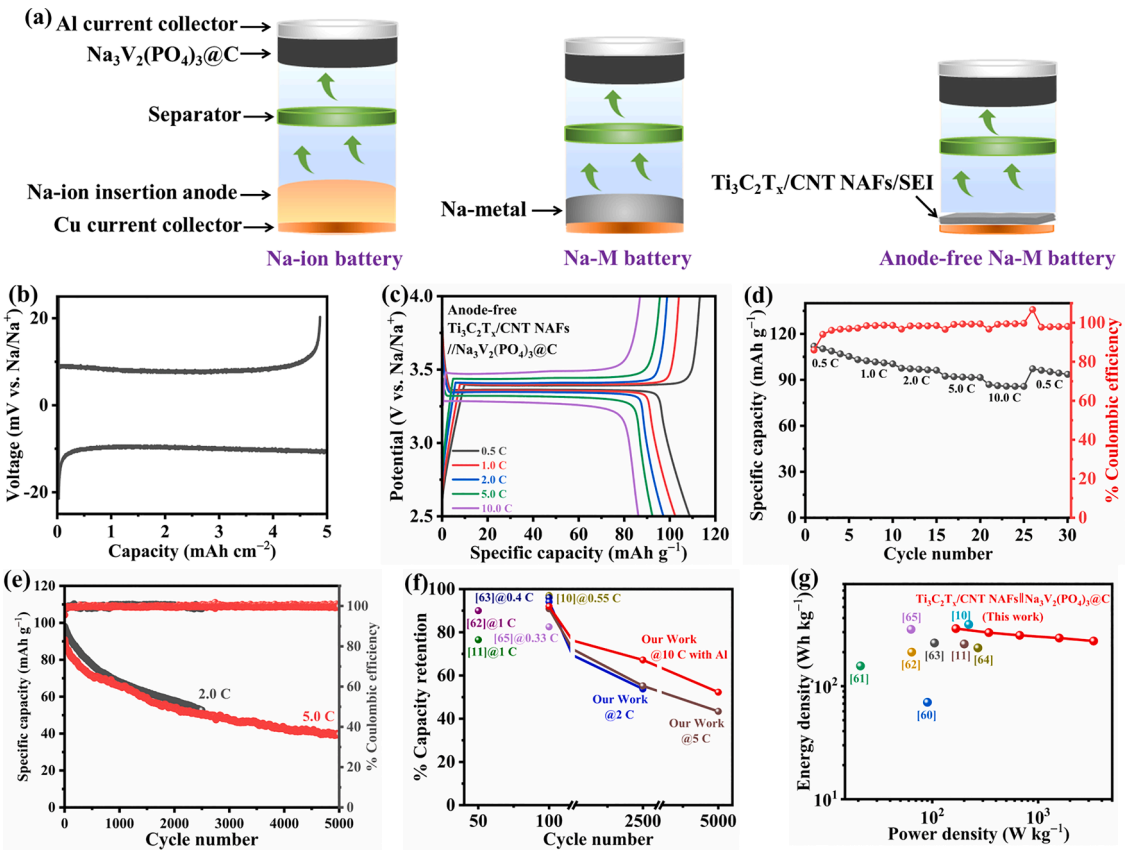

Fig. 6. (a) A schematic representation of distinctions between Na-ion, Na-M, and AFSMBs. (b) Preconditioning process of anode-free $Ti_3C_2T_x$/CNT NAFs/Na-SEI. Electrochemical full-cell performance of anode-free $Ti_3C_2T_x$/CNT NAFs/Na-SEI//$Na_3V_2(PO_4)_3$@C cell. (c) GCD plot and (d) rate capability plot at different C-rate of 0.5 C–10.0 C of the anode-free $Ti_3C_2T_x$/CNT NAFs/Na-SEI//$Na_3V_2(PO_4)_3$@C cell. (e) Cyclic stability plots of anode-free $Ti_3C_2T_x$/CNT NAFs/Na-SEI//$Na_3V_2(PO_4)_3$@C cells at 2.0 and 5.0 C. (f) Comparison of capacity retention of anode-free $Ti_3C_2T_x$/CNT NAFs/Na-SEI//$Na_3V_2(PO_4)_3$@C cells with previously reported anode-free full cells. (g) Ragone plot of anode-free $Ti_3C_2T_x$/CNT NAFs/Na-SEI//$Na_3V_2(PO_4)_3$@C full cell with previously reported $Na_3V_2(PO_4)_3$@C-based anode-less/anode-free SMBs.

observed that the capacity loss per cycle lowers drastically as the cycles progress, which is beneficial in anode-free $Ti_3C_2T_x$/CNT NAFs/Na-SEI//$Na_3V_2(PO_4)_3$@C/Cu full cells and thus resulting in better cyclic stability at high C-rates. Additionally, the CE of the anode-free $Ti_3C_2T_x$/CNT NAFs/Na-SEI//$Na_3V_2(PO_4)_3$@C cell is stably maintained at approximately 99.8 % at 5.0 C, whereas the CE of the Na//$Na_3V_2(PO_4)_3$@C cell unstably fluctuates at 2.0 and 5.0 C. The ultralong cyclic stability of anode-free $Ti_3C_2T_x$/CNT NAFs/Na-SEI//$Na_3V_2(PO_4)_3$@C cell is mainly due to that $Ti_3C_2T_x$/CNT NAFs possess exceptional sodiophilicity and efficient anode hosting characteristics for the resilient nano-accordion framework with high mechanical deformability.

The Al current collector can be used more efficiently as a practical current collector on both the cathode and anode sides because Al does not make any alloy reaction with sodium (Na) [10,17]. On the other side, Al is lighter than Cu, which can abruptly increase the cell's overall energy density. To examine the effect of the Al current collector on the anode side, we pressed the $Ti_3C_2T_x$/CNT NAFs onto an Al foil and then preconditioned the $Ti_3C_2T_x$/CNT NAFs/Al as follows: one cycle of Na plating at a capacity of 3.0 mAh cm^{-2} at a current of 1.0 mA cm^{-2} and then completely stripped to 1.0 V (Fig. S13a), with the resultant electrode serving as an anode-free host for the full cell. At 10.0 C-rate, the capacity retention of anode-free $Ti_3C_2T_x$/CNT NAFs/Al//$Na_3V_2(PO_4)_3$@C cell is determined to be 52.3 % after 5,000 cycles, with a CE that is sustainable at 99.8 % (Fig. S13b). From our experimental results, we notice better cyclic stability with the Al current collector as compared to the Cu current collector. These results indicate that $Ti_3C_2T_x$/CNT NAFs can be utilized efficiently as a dendrite-free anode host on both Cu and Al current collectors, even at a high C-rate. The anode-free $Ti_3C_2T_x$/CNT NAFs/Na-SEI//$Na_3V_2(PO_4)_3$@C/Cu and anode-free $Ti_3C_2T_x$/CNT NAFs/Al//$Na_3V_2(PO_4)_3$@C/Al full cells demonstrated remarkable cyclic stabilities in comparison to previously reported $Na_3V_2(PO_4)_3$-based anode-less/anode-free full cells (Fig. 6f, Table S3). To the best of our knowledge, this is the first time that $Ti_3C_2T_x$-based anode-free full cells have demonstrated such long-term stability at a high C-rate with outstanding CE retention. In particular, unlike other anode-free batteries that showed long-term stability of about 100 cycles at low rates, our cells showed stable CEs and capacities even after 5,000 cycles at high speeds up to 10 C.

The energy density of a battery is one of the primary factors determining battery efficiency. To calculate the energy density of the cell, the mass of $Ti_3C_2T_x$/CNT NAFs, $Na_3V_2(PO_4)_3$@C, and the deposited Na on $Ti_3C_2T_x$/CNT NAFs are utilized. Using a Ragone plot (Fig. 6g), the predicted energy density of the anode-free $Ti_3C_2T_x$/CNT NAFs/Na-SEI//$Na_3V_2(PO_4)_3$@C cell is compared to the previously reported energy densities of $Na_3V_2(PO_4)_3$@C-based AFSMBs. The energy density of the anode-free $Ti_3C_2T_x$/CNT NAFs/Na-SEI//$Na_3V_2(PO_4)_3$@C cell (N/P ratio = 0.3) is calculated to be 322.6 Wh kg^{-1} at a power density of 167.2 W kg^{-1}. Moreover, at a 10.0 C-rate, it maintains an excellent energy density of 250.7 Wh kg^{-1} at a power density of about 3,342.9 W kg^{-1}. These outcomes transcend the previously reported $Na_3V_2(PO_4)_3$@C-based anode-free/anode-less full-cell SMBs [10,11,60–65]. All of these findings illustrate the enhanced sodiophilicity of $Ti_3C_2T_x$/CNT NAFs and suggest that they can serve as an effective anode host for AFSMBs. The current research can pave the way for the future development of smart anode hosts for AFSMBs.

3. Conclusion

In summary, we have successfully developed a mechanically resilient $Ti_3C_2T_x$/CNT NAFs Na host structure via directional freezing followed by vertical compression. The $Ti_3C_2T_x$/CNT NAFs/Na asymmetric cells demonstrated excellent long-term cyclic stability, low nucleation overpotential, and better CEs. Nano-accordion structure of $Ti_3C_2T_x$/CNT NAFs confirmed compression of $Ti_3C_2T_x$/CNT NAFs during plating and expansion during stripping, suggesting their resilient nature. The symmetric cells with $Ti_3C_2T_x$/CNT NAFs exhibited very low voltage hysteresis and long-term cyclic stability without dendrite formation. Moreover, $Ti_3C_2T_x$/CNT NAFs can host a high capacity of 20.0 mAh cm^{-2} at 5 mA cm^{-2}, indicating excellent Na hosting ability. Moreover, the anode-free $Ti_3C_2T_x$/CNT NAFs/Na-SEI//$Na_3V_2(PO_4)_3$@C full cell delivered a capacity of 102.1 mAh g^{-1} at 1.0 C. Importantly, the anode-free $Ti_3C_2T_x$/CNT NAFs/Na-SEI//$Na_3V_2(PO_4)_3$@C full cell demonstrated exceptional cyclic stability at 2.0 C for 2,500 cycles and at 5.0 C for 5,000 cycles. Furthermore, the anode-free $Ti_3C_2T_x$/CNT NAFs/Al//$Na_3V_2(PO_4)_3$@C full cell also exhibits extraordinary cyclic stability at 10.0 C-rate for 5,000 cycles without cell failure. First-principles calculations further revealed that the interplay of surface chemistry and structural defects in the $Ti_3C_2T_x$/CNT NAFs significantly influences their sodiophilic properties and structural stability, enhancing the Na binding and overall performance of the cell. All of these results suggest a resilient nano-accordion structure with high sodiophilicity of $Ti_3C_2T_x$/CNT NAFs and their effective anode hosting nature towards AFSMBs. This design can pave the way for the development of smart anode hosts towards next-generation high energy density AFSMBs in the near future.

CRediT authorship contribution statement

Syam Kandula: Conceptualization, Methodology, Investigation, Writing – original draft, Funding acquisition. **Eunji Kim:** Conceptualization, Methodology, Writing – review & editing. **Chi Won Ahn:** Writing – review & editing. **Jinwoo Lee:** Writing – review & editing. **Bongjun Yeom:** Writing – review & editing. **Seung Woo Lee:** Writing – review & editing. **Jinhan Cho:** Writing – review & editing. **Hyung-Kyu Lim:** Software, Formal analysis, Writing – original draft. **Yonghee Lee:** Resources, Writing – review & editing. **Jeong Gon Son:** Conceptualization, Resources, Writing – review & editing, Funding acquisition, Supervision.

Declaration of Competing Interest

The authors declare that they have no known competing financial interests or personal relationships that could have appeared to influence the work reported in this paper.

Acknowledgment

This work was mainly supported by the Brain Pool Program through the National Research Foundation of Korea (NRF), funded by the Ministry of Science and ICT (Grant no.2019H1D3A1A01070498 and 2022R1C1C1011484). In addition, we also gratefully acknowledge financial support from the Korea Institute of Science and Technology (KIST) institutional and KU-KIST programs (Project No. 2E32501, 2E32503 and 2V09840-23-P025) and the National Research Foundation of Korea (NRF) grant funded by the Korean government (MEST) (No. NRF-2022R1A2B5B02001597). This work was also supported by the Semiconductor-Secondary Battery Interfacing Platform Technology Development Project of NNFC.

Supplementary materials

Supplementary material associated with this article can be found, in the online version, at doi:10.1016/j.ensm.2023.103024.

References

[1] B. Lee, E. Paek, D. Mitlin, S.W. Lee, Sodium metal anodes: emerging solutions to dendrite growth, Chem. Rev. 119 (2019) 5416–5460, https://doi.org/10.1021/acs.chemrev.8b00642.
[2] C. Chu, R. Li, F. Cai, Z. Bai, Y. Wang, X. Xu, N. Wang, J. Yang, S. Dou, Recent advanced skeletons in sodium metal anodes, Energy Environ. Sci. 14 (2021) 4318–4340, https://doi.org/10.1039/D1EE01341F.
[3] Z. Li, K. Zhu, P. Liu, L. Jiao, 3D confinement strategy for dendrite-free sodium metal batteries, Adv. Energy Mater. 12 (2022), 2100359, https://doi.org/10.1002/aenm.202100359.
[4] J. Pu, C. Zhong, J. Liu, Z. Wang, D. Chao, Advanced *in situ* technology for Li/Na metal anodes: an in-depth mechanistic understanding, Energy Environ. Sci. 14 (2021) 3872–3911, https://doi.org/10.1039/D1EE00110H.
[5] S. Nanda, A. Gupta, A. Manthiram, Anode-free full cells: a pathway to high-energy density lithium-metal batteries, Adv. Energy Mater. 11 (2021), 2000804, https://doi.org/10.1002/aenm.202000804.
[6] M.J. Lee, J. Han, K. Lee, Y.J. Lee, B.G. Kim, K.N. Jung, B.J. Kim, S.W. Lee, Elastomeric electrolytes for high-energy solid-state lithium batteries, Nature 601 (2022) 217–222, https://doi.org/10.1038/s41586-021-04209-4.
[7] L. Ye, M. Liao, T. Zhao, H. Sun, Y. Zhao, X. Sun, B. Wang, H. Peng, A sodiophilic interphase-mediated, dendrite-free anode with ultrahigh specific capacity for sodium-metal batteries, Angew. Chem. Int. Ed. 58 (2019) 17054–17060, https://doi.org/10.1002/anie.201910202.
[8] Z.P. Cano, D. Banham, S. Ye, A. Hintennach, J. Lu, M. Fowler, Z. Chen, Batteries and fuel cells for emerging electric vehicle markets, Nat. Energy 3 (2018) 279–289, https://doi.org/10.1038/s41560-018-0108-1.
[9] M. Bai, X. Tang, S. Liu, H. Wang, Y. Liu, A. Shao, M. Zhang, Z. Wang, Y. Ma, An anodeless, mechanically flexible and energy/power dense sodium battery prototype, Energy Environ. Sci. 15 (2022) 4686–4699, https://doi.org/10.1039/D2EE02115C.
[10] H. Li, H. Zhang, F. Wu, M. Zarrabeitia, D. Geiger, U. Kaiser, A. Varzi, S. Passerini, Sodiophilic current collectors based on MOF-derived nanocomposites for anodeless na-metal batteries, Adv. Energy Mater. 12 (2022), 2202293, https://doi.org/10.1002/aenm.202202293.
[11] K. Lee, Y.J. Lee, M.J. Lee, J. Han, J. Lim, K. Ryu, H. Yoon, B. Kim, B.J. Kim, S. W. Lee, A 3D hierarchical host with enhanced sodiophilicity enabling anode-free sodium-metal batteries, Adv. Mater. 34 (2022), 2109767, https://doi.org/10.1002/adma.202109767.
[12] F. Liang, X. Qiu, Q. Zhang, Y. Kang, A. Koo, K. Hayashi, K. Chen, D. Xue, K.N. Hui, H. Yadegari, X. Sun, A liquid anode for rechargeable sodium-air batteries with low voltage gap and high safety, Nano Energy 49 (2018) 574–579, https://doi.org/10.1016/j.nanoen.2018.04.074.
[13] X. Hu, P.H. Joo, E. Matios, C. Wang, J. Luo, K. Yang, W. Li, Designing an all-solid-state sodium-carbon dioxide battery enabled by nitrogen-doped nanocarbon, Nano Lett. 20 (2020) 3620–3626, https://doi.org/10.1021/acs.nanolett.0c00564.
[14] Y. Kim, M. Künzel, D. Steinle, X. Dong, G.T. Kim, A. Varzi, S. Passerini, Anode-less seawater batteries with a Na-ion conducting solid-polymer electrolyte for power to metal and metal to power energy storage, Energy Environ. Sci. 15 (2022) 2610–2618, https://doi.org/10.1039/D2EE00609J.
[15] J. Luo, X. Lu, E. Matios, C. Wang, H. Wang, Y. Zhang, X. Hu, W. Li, Tunable MXene-derived 1D/2D hybrid nanoarchitectures as a stable matrix for dendrite-free and ultrahigh capacity sodium metal anode, Nano Lett. 20 (2020) 7700–7708, https://doi.org/10.1021/acs.nanolett.0c03215.
[16] C. Bao, B. Wang, P. Liu, H. Wu, Y. Zhou, D. Wang, H. Liu, S. Dou, Solid electrolyte interphases on sodium metal anodes, Adv. Funct. Mater. 30 (2020), 2004891, https://doi.org/10.1002/adfm.202004891.
[17] Y. Li, Q. Zhou, S. Weng, F. Ding, X. Qi, J. Lu, Y. Li, X. Zhang, X. Rong, Y. Lu, X. Wang, R. Xiao, H. Li, X. Huang, L. Chen, Y.S. Hu, Interfacial engineering to achieve an energy density of over 200 Wh kg^{-1} in sodium batteries, Nat. Energy 7 (2022) 511–519, https://doi.org/10.1038/s41560-022-01033-6.
[18] T. Yang, D. Luo, Y. Liu, A. Yu, Z. Chen, Anode-free sodium metal batteries as rising stars for lithium-ion alternatives, iScience 26 (2023), 105982, https://doi.org/10.1016/j.isci.2023.105982.
[19] N. Lee, J. Oh, J.W. Choi, Anode-less all-solid-state batteries: recent advances and future outlook, Mater. Future 2 (2023), 013502, https://doi.org/10.1088/2752-5724/acb3e8.
[20] H. Wang, E. Matios, J. Luo, W. Li, Combining theories and experiments to understand the sodium nucleation behavior towards safe sodium metal batteries, Chem. Soc. Rev. 49 (2020) 3783–3805, https://doi.org/10.1039/D0CS00033G.
[21] M. Zhu, S. Li, B. Li, Y. Gong, Z. Du, S. Yang, Homogeneous guiding deposition of sodium through main group II metals toward dendrite-free sodium anodes, Sci. Adv. 5 (2019) eaau6264, https://doi.org/10.1126/sciadv.aau6264.
[22] L. Zhou, Z. Cao, J. Zhang, Q. Sun, Y. Wu, W. Wahyudi, J.Y. Hwang, L. Wang, L. Cavallo, Y.K. Sun, H.N. Alshareef, J. Ming, Engineering sodium-ion solvation structure to stabilize sodium anodes: universal strategy for fast-charging and safer sodium-ion batteries, Nano Lett. 20 (2020) 3247–3254, https://doi.org/10.1021/acs.nanolett.9b05355.
[23] J. Seok, J.H. Hyun, A. Jin, J.H. Um, H.D. Abruña, S.H. Yu, Visualization of sodium metal anodes via operando X-ray and optical microscopy: controlling the morphological evolution of sodium metal plating, ACS Appl. Mater. Interfaces 14 (2022) 10438–10446, https://doi.org/10.1021/acsami.1c24673.
[24] J.H. Um, S.J. Kim, J.H. Hyun, M. Kim, S.H. Lee, S.H. Yu, Real-time visualizing nucleation and growth of electrodes for post-lithium-ion batteries, Acc. Chem. Res. 56 (2023) 440–451, https://doi.org/10.1021/acs.accounts.2c00652.

[25] J. Zheng, S. Chen, W. Zhao, J. Song, M.H. Engelhard, J.G. Zhang, Extremely stable sodium metal batteries enabled by localized high-concentration electrolytes, ACS Energy Lett. 3 (2018) 315–321, https://doi.org/10.1021/acsenergylett.7b01213.

[26] J. He, A. Bhargav, W. Shin, A. Manthiram, Stable dendrite-free sodium–sulfur batteries enabled by a localized high-concentration electrolyte, J. Am. Chem. Soc. 143 (2021) 20241–20248, https://doi.org/10.1021/jacs.1c08851.

[27] D.A. Rakov, F. Chen, S.A. Ferdousi, H. Li, T. Pathirana, A.N. Simonov, P.C. Howlett, R. Atkin, M. Forsyth, Engineering high-energy-density sodium battery anodes for improved cycling with superconcentrated ionic-liquid electrolytes, Nat. Mater. 19 (2020) 1096–1101, https://doi.org/10.1038/s41563-020-0673-0.

[28] M. Bay, M. Wang, R. Grissa, M.V.F. Heinz, J. Sakamoto, C. Battaglia, Sodium plating from Na-β''-alumina ceramics at room temperature, paving the way for fast-charging all-solid-state batteries, Adv. Energy Mater. 10 (2020), 1902899, https://doi.org/10.1002/aenm.201902899.

[29] C. Bao, J. Wang, B. Wang, J. Sun, L. He, Z. Pan, Y. Jiang, D. Wang, X. Liu, S.X. Dou, J. Wang, 3D sodiophilic Ti_3C_2 MXene@g-C_3N_4 hetero-interphase raises the stability of sodium metal anodes, ACS Nano 16 (2022) 17197–17209, https://doi.org/10.1021/acsnano.2c07771.

[30] W. Luo, C. Lin, O. Zhao, M. Noked, Y. Zhang, G.W. Rubloff, L. Hu, Ultrathin surface coating enables the stable sodium metal anode, Adv. Energy Mater. 7 (2017), 1601526, https://doi.org/10.1002/aenm.201601526.

[31] J. Lee, S.H. Choi, G. Im, K. Lee, T. Lee, J. Oh, N. Lee, H. Kim, Y. Kim, S. Lee, J. W. Choi, Room-temperature anode-less all-solid-state batteries via the conversion reaction of metal fluorides, Adv. Mater. 34 (2022), 2203580, https://doi.org/10.1002/adma.202203580.

[32] Y. Wang, Y. Liu, M. Nguyen, J. Cho, N. Katyal, B.S. Vishnugopi, H. Hao, R. Fang, N. Wu, P. Liu, P.P. Mukherjee, J. Nanda, G. Henkelman, J. Watt, D. Mitlin, Stable anode-free all-solid-state lithium battery through tuned metal wetting on the copper current collector, Adv. Mater. 35 (2023), 2206762, https://doi.org/10.1002/adma.202206762.

[33] Y.J. Gong, S. Pyo, H. Kim, J. Cho, H. Yun, H. Kim, S. Ryu, J. Yoo, Y.S. Kim, Advanced Li metal anode by fluorinated metathesis on conjugated carbon networks, Energy Environ. Sci. 14 (2021) 940–954, https://doi.org/10.1039/D0EE02827D.

[34] Y.J. Gong, J.W. Heo, H. Lee, H. Kim, J. Cho, S. Pyo, H. Yun, H. Kim, S.Y. Park, J. Yoo, Y.S. Kim, Nonwoven rGO fiber-aramid separator for high-speed charging and discharging of Li metal anode, Adv. Energy Mater. 10 (2020), 2001479, https://doi.org/10.1002/aenm.202001479.

[35] M. Naguib, M.W. Barsoum, Y. Gogotsi, Ten years of progress in the synthesis and development of MXenes, Adv. Mater. 33 (2021), 2103393, https://doi.org/10.1002/adma.202103393.

[36] F. Ming, H. Liang, G. Huang, Z. Bayhan, H.N. Alshareef, MXenes for rechargeable batteries beyond the lithium-ion, Adv. Mater. 33 (2021), 2004039, https://doi.org/10.1002/adma.202004039.

[37] A. Iqbal, P. Sambyal, C.M. Koo, 2D MXenes for electromagnetic shielding: a review, Adv. Funct. Mater. 30 (2020), 2000883, https://doi.org/10.1002/adfm.202000883.

[38] H. Shi, M. Yue, C.J. Zhang, Y. Dong, P. Lu, S. Zheng, H. Huang, J. Chen, P. Wen, Z. Xu, Q. Zheng, X. Li, Y. Yu, Z.S. Wu, 3D flexible, conductive, and recyclable $Ti_3C_2T_x$ MXene-melamine foam for high-areal-capacity and long-lifetime alkali-metal anode, ACS Nano 14 (2020) 8678–8688, https://doi.org/10.1021/acsnano.0c03042.

[39] E. Kim, J. Song, T.E. Song, H. Kim, Y.J. Kim, Y.W. Oh, S. Jung, I.S. Kang, Y. Gogotsi, H. Han, C.W. Ahn, Y. Lee, Scalable fabrication of MXene-based flexible micro-supercapacitor with outstanding volumetric capacitance, Chem. Eng. J. 450 (2022), 138456, https://doi.org/10.1016/j.cej.2022.138456.

[40] J. Luo, C. Wang, H. Wang, X. Hu, E. Matios, X. Lu, W. Zhang, X. Tao, W. Li, Pillared MXene with ultralarge interlayer spacing as a stable matrix for high performance sodium metal anodes, Adv. Funct. Mater. 29 (2019), 1805946, https://doi.org/10.1002/adfm.201805946.

[41] X. He, S. Jin, L. Miao, Y. Cai, Y. Hou, H. Li, K. Zhang, Z. Yan, J. Chen, A 3D Hydroxylated MXene/carbon nanotubes composite as a scaffold for dendrite-free sodium-metal electrodes, Angew. Chemie Int. Ed. 59 (2020) 16705–16711, https://doi.org/10.1002/anie.202006783.

[42] Y. Fang, R. Lian, H. Li, Y. Zhang, Z. Gong, K. Zhu, K. Ye, J. Yan, G. Wang, Y. Gao, Y. Wei, D. Cao, Induction of planar sodium growth on MXene ($Ti_3C_2T_x$)-Modified carbon cloth hosts for flexible sodium metal anodes, ACS Nano 14 (2020) 8744–8753, https://doi.org/10.1021/acsnano.0c03259.

[43] H. Jiang, X. Lin, C. Wei, Y. Zhang, J. Feng, X. Tian, Sodiophilic Mg^{2+}-decorated Ti_3C_2 MXene for dendrite-free sodium metal batteries with carbonate-based electrolytes, Small 18 (2022), 2107637, https://doi.org/10.1002/smll.202107637.

[44] S. Wang, Y. Liu, K. Lu, W. Cai, Y. Jie, F. Huang, X. Li, R. Cao, S. Jiao, Engineering rGO/MXene hybrid film as an anode host for stable sodium-metal batteries, Energy Fuels 35 (2021) 4587–4595, https://doi.org/10.1021/acs.energyfuels.0c04408.

[45] D. Seo, M. Kim, J. Kyu Song, E. Kim, J. Koo, K. Kim, H. Han, Y. Lee, C. Won Ahn, Hollow Ti_3C_2 MXene/carbon nanofibers as an advanced anode material for lithium-ion batteries, ChemElectroChem. 9 (2022), e20210134, https://doi.org/10.1002/celc.202101344.

[46] H. Chen, A. Pei, J. Wan, D. Lin, R. Vilá, H. Wang, D. Mackanic, H.G. Steinrück, W. Huang, Y. Li, A. Yang, J. Xie, Y. Wu, H. Wang, Y. Cui, Tortuosity effects in lithium-metal host anodes, Joule 4 (2020) 938–952, https://doi.org/10.1016/j.joule.2020.03.008.

[47] C.E. Shuck, A. Sarycheva, M. Anayee, A. Levitt, Y. Zhu, S. Uzun, V. Balitskiy, V. Zahorodna, O. Gogotsi, Y. Gogotsi, Scalable synthesis of $Ti_3C_2T_x$ MXene, Adv. Eng. Mater. 22 (2020), 1901241, https://doi.org/10.1002/adem.201901241.

[48] J. Yan, C.E. Ren, K. Maleski, C.B. Hatter, B. Anasori, P. Urbankowski, A. Sarycheva, Y. Gogotsi, Flexible MXene/graphene films for ultrafast supercapacitors with outstanding volumetric capacitance, Adv. Funct. Mater. 27 (2017), 1701264, https://doi.org/10.1002/adfm.201701264.

[49] M.S. Dresselhaus, G. Dresselhaus, R. Saito, A. Jorio, Raman spectroscopy of carbon nanotubes, Phys. Rep. 409 (2005) 47–99, https://doi.org/10.1016/j.physrep.2004.10.006.

[50] S. Kandula, J. Bae, J. Cho, J.G. Son, Gram-scale synthesis of rGO wrapped porous α-Fe_2O_3 as an advanced anode material for Na-ion batteries with superior cyclic stability, Compos. Part B Eng. 220 (2021), 108995, https://doi.org/10.1016/j.compositesb.2021.108995.

[51] S. Kandula, B. Sik Youn, J. Cho, H.K. Lim, J. Gon Son, FeS_2@N-C nanorattles encapsulated in N/S dual-doped graphene/carbon nanotube network composites for high performance and high rate capability anodes of sodium-ion batteries, Chem. Eng. J. 439 (2022), 135678, https://doi.org/10.1016/j.cej.2022.135678.

[52] V. Natu, M. Benchakar, C. Canaff, A. Habrioux, S. Célérier, M.W. Barsoum, A critical analysis of the X-ray photoelectron spectra of $Ti_3C_2T_z$ MXenes, Matter 4 (2021) 1224–1251, https://doi.org/10.1016/j.matt.2021.01.015.

[53] M. Benchakar, L. Loupias, C. Garnero, T. Bilyk, C. Morais, C. Canaff, N. Guignard, S. Morisset, H. Pazniak, S. Hurand, P. Chartier, J. Pacaud, V. Mauchamp, M. W. Barsoum, A. Habrioux, S. Célérier, One MAX phase, different MXenes: a guideline to understand the crucial role of etching conditions on $Ti_3C_2T_x$ surface chemistry, Appl. Surf. Sci. 530 (2020), 147209, https://doi.org/10.1016/j.apsusc.2020.147209.

[54] H. Kim, J. Kee, D.R. Seo, Y. Lee, C.W. Ahn, J. Koo, Large-area 2D-MXene nanosheet assemblies using Langmuir–Schaefer technique: wrinkle formation, ACS Appl. Mater. Interfaces 12 (2020) 42294–42301, https://doi.org/10.1021/acsami.0c10990.

[55] B.D. Adams, J. Zheng, X. Ren, W. Xu, J. Zhang, Accurate determination of coulombic efficiency for lithium metal anodes and lithium metal batteries, Adv. Energy Mater. 8 (2018), 1702097, https://doi.org/10.1002/aenm.201702097.

[56] G.G. Eshetu, T. Diemant, S. Grugeon, R.J. Behm, S. Laruelle, M. Armand, S. Passerini, In-depth interfacial chemistry and reactivity focused investigation of lithium–imide- and lithium–imidazole-based electrolytes, ACS Appl. Mater. Interfaces 8 (2016) 16087–16100, https://doi.org/10.1021/acsami.6b04406.

[57] B. Qin, A. Schiele, Z. Jusys, A. Mariani, T. Diemant, X. Liu, T. Brezesinski, R. J. Behm, A. Varzi, S. Passerini, Highly reversible sodiation of tin in glyme electrolytes: the critical role of the solid electrolyte interphase and its formation mechanism, ACS Appl. Mater. Interfaces 12 (2020) 3697–3708, https://doi.org/10.1021/acsami.9b20616.

[58] J. Um, S.U. Yoon, H. Kim, B.S. Youn, H.J. Jin, H.K. Lim, Y.S. Yun, High-performance solid-solution potassium-ion intercalation mechanism of multilayered turbostratic graphene nanosheets, J. Energy Chem. 67 (2022) 814–823, https://doi.org/10.1016/j.jechem.2021.11.027.

[59] M. Xia, C. Liang, Z. Cheng, R. Hu, S. Liu, The adhesion energy measured by a stress accumulation-peeling mechanism in the exfoliation of graphite, Phys. Chem. Chem. Phys. 21 (2019) 1217–1223, https://doi.org/10.1039/C8CP06608F.

[60] G. Wang, Y. Zhang, B. Guo, L. Tang, G. Xu, Y. Zhang, M. Wu, H.K. Liu, S.X. Dou, C. Wu, C. Wu, Core-Shell C@Sb nanoparticles as a nucleation layer for high-performance sodium metal anodes, Nano Lett. 20 (2020) 4464–4471, https://doi.org/10.1021/acs.nanolett.0c01257.

[61] N. Wang, Z. Bai, Y. Qian, J. Yang, Double-walled Sb@TiO_{2-x} nanotubes as a superior high-rate and ultralong-lifespan anode material for Na-Ion and Li-ion batteries, Adv. Mater. 28 (2016) 4126–4133, https://doi.org/10.1002/adma.201505918.

[62] B. Zhang, G. Rousse, D. Foix, R. Dugas, D.A.D. Corte, J.M. Tarascon, Microsized Sn as advanced anodes in glyme-based electrolyte for Na-ion batteries, Adv. Mater. 28 (2016) 9824–9830, https://doi.org/10.1002/adma.201603212.

[63] T. Li, J. Sun, S. Gao, B. Xiao, J. Cheng, Y. Zhou, X. Sun, F. Jiang, Z. Yan, S. Xiong, Superior sodium metal anodes enabled by sodiophilic carbonized coconut framework with 3D tubular structure, Adv. Energy Mater. 11 (2021), 2003699, https://doi.org/10.1002/aenm.202003699.

[64] X.Y. Cui, Y.J. Wang, H.D. Wu, X.D. Lin, S. Tang, P. Xu, H.G. Liao, M. Sen Zheng, Q. F. Dong, A carbon foam with sodiophilic surface for highly reversible, ultra-long cycle sodium metal anode, Adv. Sci. 8 (2021), 2003178, https://doi.org/10.1002/advs.202003178.

[65] A.P. Cohn, T. Metke, J. Donohue, N. Muralidharan, K. Share, C.L. Pint, Rethinking sodium-ion anodes as nucleation layers for anode-free batteries, J. Mater. Chem. A 6 (2018) 23875–23884, https://doi.org/10.1039/C8TA05911J.